Solar Eruptive Events:

Coronal Dimming and a New CubeSat Mission

by

James Paul Mason

B.S., University of California at Santa Cruz, 2009

M.S., University of Colorado at Boulder, 2012

A thesis submitted to the

Faculty of the Graduate School of the

University of Colorado in partial fulfillment

of the requirements for the degree of

Doctor of Philosophy

Department of Aerospace Engineering Sciences

2016

This thesis entitled:

Solar Eruptive Events:

Coronal Dimming and a New CubeSat Mission

written by James Paul Mason

has been approved for the Department of Aerospace Engineering Sciences

Dr. Thomas Woods

Prof. Xinlin Li

Prof. Scott Palo

Dr. Amir Caspi

Prof. Jeffrey Forbes

Date

The final copy of this thesis has been examined by the signatories, and we find that both the content and the form meet acceptable presentation standards of scholarly work in the above mentioned discipline.

Mason, James Paul (Ph.D., Aerospace Engineering Sciences)

Solar Eruptive Events:

Coronal Dimming and a New CubeSat Mission

Thesis directed by Dr. Thomas Woods

Often the abstract will be long enough to require more than one page, in which case the macro “\OnePageChapter” should *not* be used.

But this one isn’t, so it should.

Dedication

To my late father, who inspired me from an early age to come this far.

Acknowledgements

First and foremost, my deepest thanks to Tom Woods. Through the projects he's introduced me to – in solar physics, in sounding rockets, and in small satellites – I've discovered a career path that excites me and that provides continuous opportunities to learn and contribute. Moreover, he's an excellent role model: dedicated and passionate about his work, patient with everyone without seeming to have to try, and exceptionally reliable. All of the above combined has made my time in graduate school likely to be, upon reflection long from now, one of the highlights of my life. Thank you to my committee for guidance and support, most of whom I've been fortunate to work with closely: Xinlin Li, Scott Palo, Amir Caspi, and Jeff Forbes. Finally, I couldn't have struggled through without the support of my peers, especially Allison Youngblood, whose work ethic inspires me and whom I've been extremely lucky to find. Oh, and my dog, Nessie, who requires three walks a day, has turned out to provide the periods of relaxation away from a screen that have aided in my ability to actually comprehend the work I'm doing.

Contents

Tables

Table

Figures

Figure

Chapter 1

Introduction

- Solar eruptive events are rapid releases of energy on the Sun that are sometimes directed Earth-ward, making it important to understand them and to forecast their arrival time and magnitude of their impact

- Three basic types of eruptive event: flare, coronal mass ejection, energetic particles this dissertation focuses on the first two

- Some background about solar flare prediction provided in Chapter 2, including my own massive statistical study, which went to print in ApJ my first year of graduate school

- The relationship between coronal mass ejections and the void they leave behind in the solar corona is the primary topic of the dissertation and its discussion spans several chapters.

  * Chapter 3 discusses the various physical processes that can lead to an observation that may be interpreted as a dimming, and the amalgamation of related observations that can theoretically be used to identify and isolate each mechanism

  * Chapter 4 puts theory to the test in a detailed case study of a single, relatively simple, event. The aforementioned conglomeration of observations were used to determine that this was indeed a simple case with one dimming mechanism dominating the observation; that which theory says should be most strongly related to the associated CME

    - * Chapter 5 expands the study of the relationship between dimming and CMEs by performing an analysis similar to that of the case study but for approximately 30 events. Thus, a tentative statistical correlation between dimming and CME parameterizations could be derived.

- The topic of solar flares is picked up again briefly in the science motivation for the solar CubeSat MinXSS. An overview of the mission is the topic of Chapter 6, which includes science motivation, system overview, and lessons learned.

- Chapter 7 delves deeper into the CubeSat engineering with a detailed thermal balance test and model analysis, culminating in the (likely) first ever tuned CubeSat thermal model that has been validated by dedicated testing and on-orbit measurements.

- Chapter 8 provides a summary of deliverables and results, and lays out plans for future work. The latter will be the first steps in my post-doc that has already been secured through my first grant being funded as well as SDO/EVE and MinXSS extended mission funding.

Chapter 2

Relevant Background

2.1 Solar Corona

2.2 Physics of Solar Eruptive Event Initiation

2.3 Space Weather

2.4 EUV Emission

Maxwellian plasma versus not. Focus herein will be on Maxwellian plasmas as the studies don't focus on super hot plasmas.

2.5 Instrument Descriptions

Table 2.1: Selected emission lines

Ion	Wavelength (Å)	Peak formation temperature (MK)
Fe IX	171	0.06
Fe X	177	0.05
Fe XI	180	0.04
Fe XII	195	0.04
Fe XIII	202	0.04
Fe XIV	211	0.07
Fe XV	284	0.08
Fe XVI	335	0.17
Fe XVIII	94	0.08
Fe XX	132	0.20

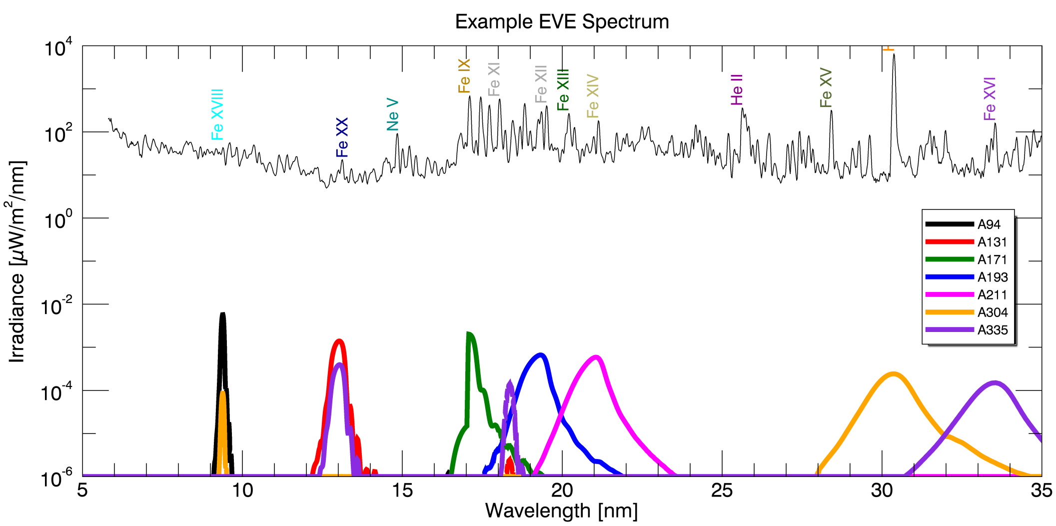

Figure 2.1: AIA bandpasses, model solar spectrum to provide an idea of the amount of blending.

Chapter 3

Mechanisms and Observational Signatures of Coronal Dimming

This chapter details the physics of coronal dimming and the observational signatures that result. There are theoretically many physical processes that can lead to an observer identifying "dimming", but some physical processes have little to do with a coronal mass ejection (CME). Traditionally, the term "coronal dimming" has been assumed to refer to the void left in the corona after a CME departs. This is one cause of a transient hole in the corona and is of the greatest concern to space weather forecasters. However, changing temperatures (common during solar eruptive events) cause ionization fraction shifting, resulting in some emissions dimming while others brighten. Additionally, dark material (e.g., a filament) can pass between a lower bright region (e.g., flaring loops) and the observer, causing a transient dip in emission. Third, solar eruptive events sometimes have associated waves that propagate across the solar disk. These waves are observed as narrow bright fronts with a trailing dark region. The trailing dark region is another way to achieve a transient dimming of emission. Next, there are two ways that Doppler effects can cause transient dips in emission. The first is called Doppler dimming and results from fast moving plasma being sufficiently Doppler-shifted to reduce resonant fluorescence from the solar emission line sources; a phenomenon which is independent of the observation angle. The second occurs if eruptive plasma is moving fast enough in the line-of-sight to shift its emissions outside the bandpass of an observing instrument, which we have named "bandpass dimming". The physics and instrumental identifiers for each of these types of theoretically observable dimming are summarized in Table 3.1 and are discussed in detail in the sections that follow.

Table 3.1: Summary of physical processes that can manifest as observed dimming

Short Name	Physical Process	EVE Full-Disk Observational Identifiers	AIA Imaging Observational Identifiers
Mass loss (Fig. 3.1)	Ejection of emitting plasma from corona	Simultaneous intensity decrease in multiple coronal emission lines, with percentage decrease indicative of percentage mass lost	Area over and near the erupting active region (AR) darkens
Thermal (Fig. 3.2)	Heating raises ionization states (e.g., a fraction of Fe IX becomes Fe X); cooling does the opposite	Heating: Emission loss in lines with lower peak formation temperatures and near simultaneous emission gain in lines with higher peak formation temperatures; vice versa for cooling	Heating: Area near AR darkens in channels with lower peak formation temperature and near simultaneous brightening in channels with higher peak formation temperatures; vice versa for cooling
Obscuration (Fig. 3.5)	Dim feature (e.g., filament material) moves into line-of-sight over a bright feature (e.g., flare arcade)	Drop of emission lines proportional to their absorption cross section in the obscuring material	Direct observation of this obscuration process
Wave (Fig. 3.7)	Wave disturbance propagates globally, causing compression/rarefaction of plasma as wave passes by	No effects have been clearly identified	Direct observation of this wave process, especially apparent with difference movies
Doppler (Fig. 3.8)	Fast moving plasma Doppler shifts away from resonant fluorescence with solar emission lines	Doppler wavelength shift of emission lines and change in intensity, possibly also observed as line broadening	Change in intensity of moving plasma as its velocity changes
Bandpass (Fig. 3.9)	Emissions from fast moving plasma have Doppler wavelength shift	Emission line shifts in wavelength or has broadening	Doppler shift convolves with band-pass sensitivity to cause apparent reduction in emission

3.1 Mass-loss Dimming

The physical process in mass-loss dimming is the eruption of emitting plasma (see Figure 3.1; Harrison and Lyons 2000; Harra and Sterling 2001). It can be a CME (i.e., plasma leaves the sun) or a failed ejection (i.e., plasma rises and then falls back onto the sun), the latter of which still manifests locally as a mass-loss dimming, but does not result in the appearance of a CME in coronagraph data and may not appear in a disk-integrated spectrograph like EVE. The eruption physics model is the standard CME initiation discussed in Section **??**. However, where most CME discussions will then follow the CME as it transitions away from the sun into an interplanetary CME, in mass-loss dimming we are instead interested in the details of the void left behind in the corona. The mass of an average CME and a typical active region are of the same order of magnitude: 10^{15} g, meaning that a departing CME can "blow out" a large part of the active region with it (Aschwanden et al., 2009a). This is the physical process assumed to be the main contributor to observed dimming in many recent studies (Sterling and Hudson, 1997; Reinard and Biesecker, 2008, 2009; Aschwanden et al., 2009a). Harrison et al. (2003) showed that dimmings can account for a large percentage of CME mass. Thus, mass-loss dimming is very relevant for the space weather community, who study and forecast CMEs.

Observationally, mass-loss dimming appears in EVE as multiple emission lines dropping nearly simultaneously. In the case of a failed ejection, the dimming area and the ejected material are likely to maintain a total emission that is close enough to constant that it will not be apparent in EVE data. For space weather, this is of little concern since CMEs have far greater geoeffectiveness than short-lived holes in the corona of small spatial extent. However, AIA data allow the identification of mass-loss dimming even if the event is a failed ejection. In either case, mass-loss dimming appears in AIA as a relatively compact area near an active region becoming darker, sometimes with a dark cloud visibly moving off-disk. Assuming the dimmings in Reinard and Biesecker (2008) to all be due to mass loss, the timescale of the process is 3 - 12 hr and rarely persists longer than a day. Additional observations from the Hinode spacecraft have confirmed density decreases with accompanying outflows (Attrill et al., 2010; Harra et al., 2010; Tian et al., 2012).

3.2 Thermal Dimming

Temperature evolution of emission lines is only interpreted as observed dimming if one is not careful to observe co-spatial emission lines at different peak formation temperatures. As plasma is heated or cooled, the ionization fraction changes, necessarily causing the emission intensity to change (Figure 3.2). For example, heating causes some Fe IX to become Fe X and thus, in the absence of competing physical processes, Fe IX 171 Å emission drops while Fe X 177 Å emission rises. This pattern was identified observationally in Figure 6 of Woods et al. (2011) using SDO/EVE data, Robbrecht and Wang (2010) using STEREO/EUVI, and Jin et al. (2009) and Imada et al. (2007) with Hinode/EIS. It can also be observed in the standard composite (multi-wavelength) movies produced by the AIA team; indeed, this is one of the prime purposes for the composites. The initiation time and duration of temperature evolution tends to be quite similar to mass-loss dimming, as they are typically both responses to the rapid release of magnetic field energy

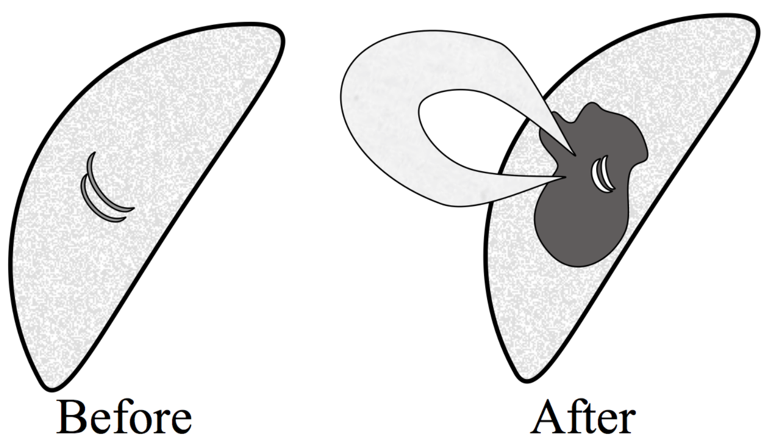

Figure 3.1: Schematic depicting the process of mass-loss dimming. Prior to the eruption (left), coronal loops between two active regions are relatively quiescent. During and after the eruption (right), the loops become brighter and reconfigured, a CME is ejected, and a void forms in the coronal plasma. The post-flare coronal loops usually reform in much the same as the original configuration.

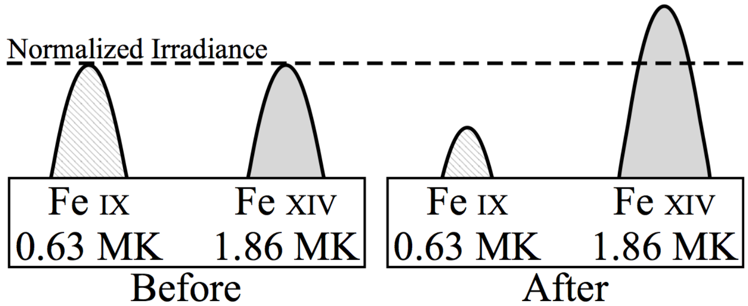

Figure 3.2: Schematic depicting the observational behavior for the thermal dimming effect. Relative to a pre-eruption time (left), the cooler Fe IX emission drops while the warmer Fe XIV emission increases (right) due to heating of the plasma and redistribution of ionization states.

in active regions and require several hours of recovery time. Thus, thermal processes could be mistaken for mass loss if only a single spectral line was observed. Ideally, unblended emission lines from an entire coronal ionization sequence (e.g., Fe I to Fe XVIII) could be used to mitigate this convolution of dimming observations. However, as we will show in Section 4.3, it may be sufficient to have observations of two sufficiently separated ionizations states to differentiate between thermal evolution and mass-loss dimming. This is due, in part, to the fact that hotter lines (e.g., Fe XV and above) are primarily emitted from confined loops near the flare and are thus not strongly impacted by mass-loss dimming.

Multi-wavelength Doppler studies have shown that while all (measured) emission lines become blue-shifted (indicating an outflow), the magnitude of the shift is strongly proportional to the lines peak formation temperature (Imada et al., 2007; Jin et al., 2009). Figure 3.3 shows this dependence for a plage region with a dimming event during an X-class flare. Part of the explanation for this is that as a population of ions is accelerated outward as part of the CME, it is simultaneously experiencing heating as part of the eruptive process. This causes the ionization fraction to shift upward to the point where there may be little low ionization states left e.g., Fe IX. Tracking a single ion, one would see the same nuclei accelerating outward while having electrons stripped away. This explains why lower ionization states seem to have relatively little outflow velocity. Additionally, Fe IX 171 Å emission can be depressed further after open magnetic field lines from the departing CME

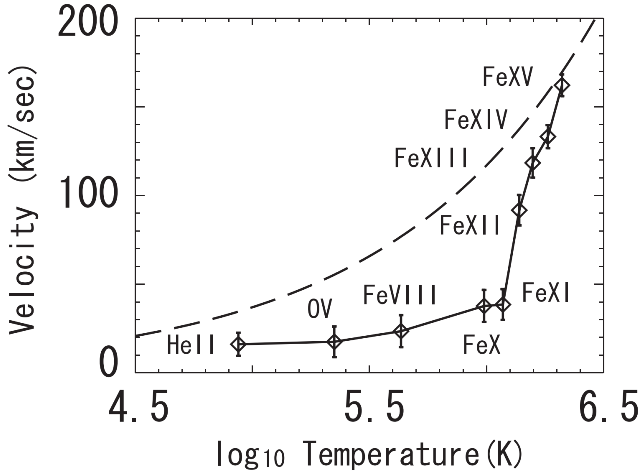

Figure 3.3: Outflow velocity vs emission line peak formation temperature for a dimming region near a plage. Adapted from Imada et al. (2007).

close down and cause another bout of heating; causing e.g., Fe IX to become Fe X and beyond, which propagates outward as a "heat wave dimming" (Robbrecht and Wang, 2010). However, Mason et al. (2014) found that the onset time, slope, and duration of dimming are comparable in SDO/AIA 171 Å and 193 Å[1] and in SDO/EVE 171Å and 195 Å (described in Chapter 4). It should also be noted that EUV images tend to provide higher contrast for dimming in Fe XII 195 Å than Fe IX 171 Å. This is because there is much less Fe XII in the quiescent corona than Fe IX. Therefore, the background in 171 Å images is much brighter, making dimming (which are typically less than a 5% reduction of full-disk emission) more difficult to identify. Nevertheless, we find that for full-disk emission (i.e., irradiance from EVE) the 171 Å emission shows stronger dimming than the 195 Å emission as shown in 3.4.

It is important to note that, in general, the magnitude of total observed dimming in a given line in EVE spectra is inversely proportional to its peak formation temperature, which can be inferred from Figure 3.4. This figure was generated using a simple algorithm that searched all EVE/MEGS-A data for relative irradiance decreases greater than a specified threshold (1%, 2%,

[1] Note that the SDO/AIA 193 Å band encompasses 195 Å

3%) of flares exceeding GOES X-ray class of C1. The window of time searched was bounded by the GOES event start time and the sooner of either 4 hours after the start time or the next GOES event start time. This algorithm was applied to all EVE data from mission start (2010 May 1) to the failure of the MEGS-A detector (due to a shorted capacitor on 2014 April 30). MEGS-A takes the measurements of all wavelengths studied here. Figure 3.4 shows that the number of dimmings dramatically decreases as the magnitude threshold is increased, and decreases slightly with higher peak formation temperature. This latter effect is partially due to flare heating adding emission in the higher temperature, higher ionization state, lines that partially offsets the mass-loss dimming. Additionally, these trends indicate that at sufficiently high peak formation temperature, no dimming may be observed at all, even at the lowest detection threshold, which is consistent with the hotter lines being restricted to the confined flare loops and hence experiencing no mass loss. In other words, the higher the peak formation temperature, the greater the relative contribution of more confined loops to the measured emission.

An instrument with spatial resolution like AIA can be used to isolate the confined flaring loops and create a time series of just the dimming region, and then the sum of those dimming regions can be compared to the EVE full-disk (irradiance) dimming trend. This type of analysis and comparison between AIA and EVE dimming is provided in Chapter 4. AIA too has its own limitations; relevant in this case is the relatively lower spectral resolution that blends together emission from several ionization states of Fe. With EVE and AIA combined, it is possible to analyze thermal dimming but the ideal instrument for fully characterizing this phenomenon would be a high spectral resolution hyperspectral imager in the EUV.

3.3 Obscuration Dimming

The physical process that results in apparent dimming here is material that is dark in a particular wavelength (e.g., a filament) moving between lower-down bright material (e.g., flare arcade) and the observer (Figure 3.5). In optically thick wavelengths, the dark plasma absorbs some of the bright emission, resulting in an apparent decrease in emission. The slow draining of plasma

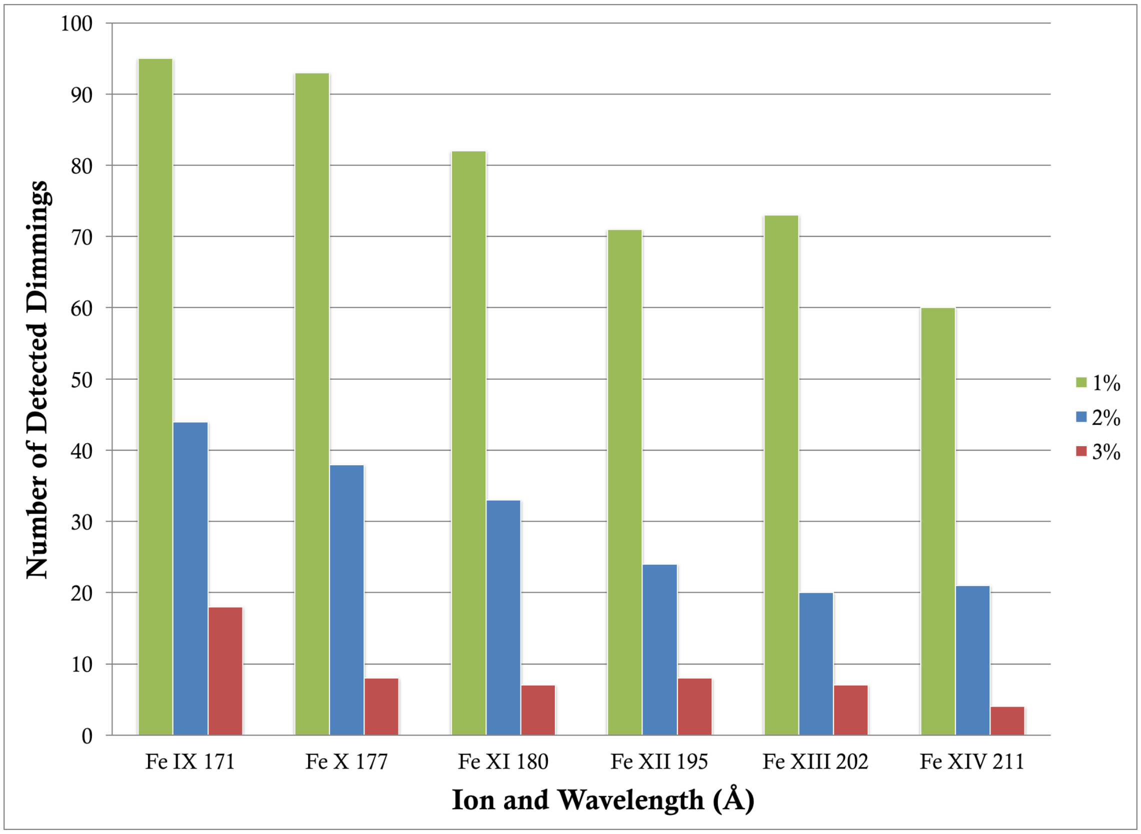

Figure 3.4: Number of identified dimmings in EVE for six spectral lines using different percentage dimming depths as the threshold for a detection. There were 302 flares ($\geq$ M1.0 GOES class) used to trigger an automated search for dimming in EVE. Note the decrease in detections with increasing ionization state (i.e. peak formation temperature).

back to the corona can obscure underlying emission for hours, and absorption can be observed in both coronal and chromospheric lines (e.g., Gilbert et al. 2013). Although obscuration dimmings can exhibit time and spatial scales comparable to the more short-lived mass-loss dimmings, it is fairly straightforward to identify absorption signatures in the EUV images. It may also be possible to identify this phenomenon with EVE using the He II 256 Å and 304 Å chromospheric emission lines and knowledge of the absorption cross-section through filamentary plasma. Figure 3.6 shows the photoionization cross-sections of the dominant species in the solar corona. Hydrogen and helium contribute an order-of-magnitude more absorption than metals[2] , and thus the effect of metals can

[2] "Metals" in the astrophysical sense

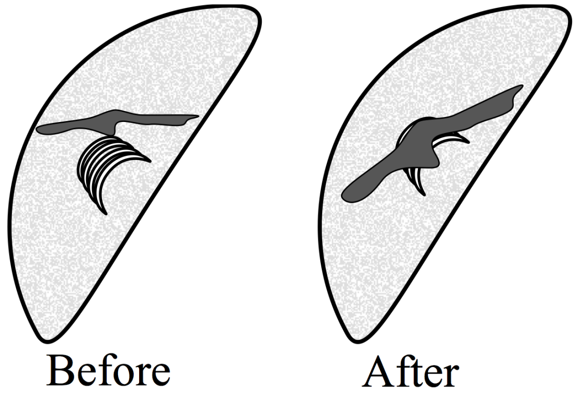

Figure 3.5: Schematic depicting the process of obscuration dimming. A filament previously obscuring only the quiet sun (left) expands and moves in front of a flare arcade (right). This results in a decreased observed emission from the flare arcade in wavelengths where the filament is optically thick.

be ignored. The cross-sections are quite steep in the wavelength range of interest here (roughly 150-310 Å). This means that approximately twice as much He II 256 Å than He II 304 Å emission will come through a filament. Furthermore, the mass-loss dimming sensitive lines (e.g., Fe IX 171 Å and 195Å) will be less affected by this obscuration, but a 1% effect would be sufficient to cause a "false" detection. It may be possible to identify obscuration dimming with EVE's 256 Å and 304 Å measurements and determine that an obscuration dimming has occurred. However, further analysis of this type of dimming is required before any conclusions can be drawn.

3.4 Wave Dimming

The debate about the physics of coronal EUV waves continues (e.g., Zhukov and Auchère 2004; Muhr et al. 2011; Liu and Ofman 2014) but one of the simplest explanations of the observations is that plasma is compressed as a longitudinal wave passes through the medium. Traveling (i.e., not static) rarefactions are sometimes observed following the compression (Muhr et al., 2011), the compressed regions having higher densities resulting in increased emission, and vice versa (Figure 3.7). Alternatively, some models suggest that the observed phenomenon is not a wave at all, but rather the impact of the CME departing on the global magnetic field (Chen et al., 2002,

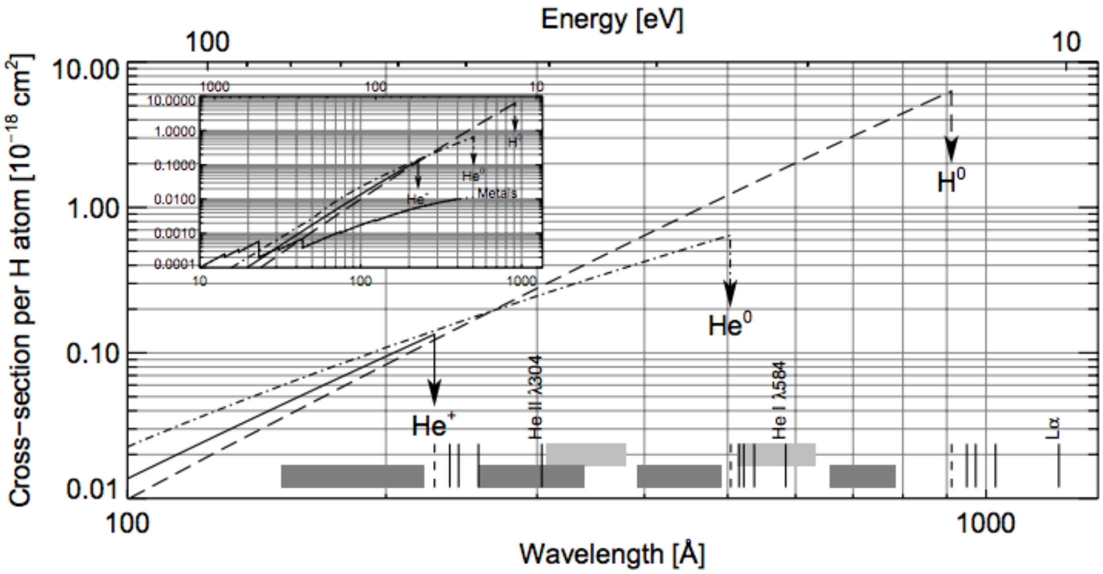

Figure 3.6: Photoionization cross-sections for He I (dot-dashed line), He II (solid line), and H (dashed line) per hydrogen atom. The inset shows a wider wavelength range of the same data but with metals shown for comparison. The dashed vertical bars at the bottom indicate the edges of respective continua. The grey regions at the bottom are not pertinent here as they correspond to specifics of the SOHO/CDS instrument. Adapted from Andretta et al. (2003).

2005). Regardless of the physical process responsible, the observation is the same. The EUV waves emanating from an eruption can be seen to cause dimmings and brightenings elsewhere in the solar EUV images, often starting at the eruption site and then seen later very far from the original eruption site, particularly near other active regions. We refer to these dimmings that are non-local to the erupting site as sympathetic dimmings (Schrijver and Higgins, 2015). This is quite likely to occur if a distant active region has significant potential energy stored when the disturbance reaches it – the wave propagating across the magnetic field lines acts as a catalyst.

It is important to distinguish between the wave-caused dimmings and other causes of remote dimming, such as large-scale disappearing loops that are visible in soft X-ray images but only have visible EUV changes at their footpoints (Pohjolainen et al., 2005). EUV wave dimmings are unlikely to be easily identified in full-disk spatially-integrated instruments like EVE because the enhanced emission nearly cancels out the dimmed emission when summed.

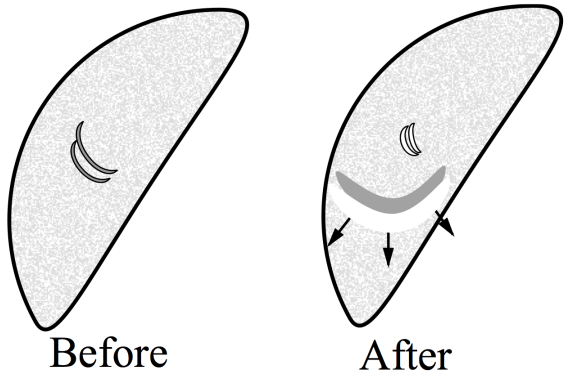

Figure 3.7: Similar to Figure 3.5, but depicting the process of wave dimming. After an eruptive event, a wave propagates and expands through the corona. The compressed plasma of the wavefront results in enhanced emission, while the rarefied trailing region is dimmed.

3.5 Doppler and Bandpass Dimming

Two additional processes can theoretically lead to the observation of dimming in a limited wavelength range and both result from Doppler effects. The first has been given the name "Doppler dimming". In this type of dimming, resonant fluorescence of a high-velocity, remote cloud of plasma (e.g., CME) by a source population (solar emission lines) can decrease as the resultant Doppler shift becomes sufficiently large (see Figure 3.8; Hyder and Lites 1970). Here, Doppler takes effect due to the relative velocity between the source (the sun) and the scattering medium (the CME) and is thus independent of observer angle. This phenomenon has been known for decades for cometary emissions (Swings, 1941; Greenstein, 1958) and has been documented in chromospheric lines associated with eruptions (Labrosse and Mcglinchey, 2012) as well as in coronal lines such as O VI for polar coronal hole outflows (Giordano et al., 2000). However, the majority of EUV emission lines in the corona are collisionally dominated i.e. not resonantly excited, and will not exhibit this effect. Furthermore, the dimming region is the CME itself, which is likely to be outside the field of view of EUV instruments observing the solar disk. Therefore, it is possible to diagnose this type of dimming when it is pronounced in resonantly excited lines but does not manifest in the lines of interest studied herein.

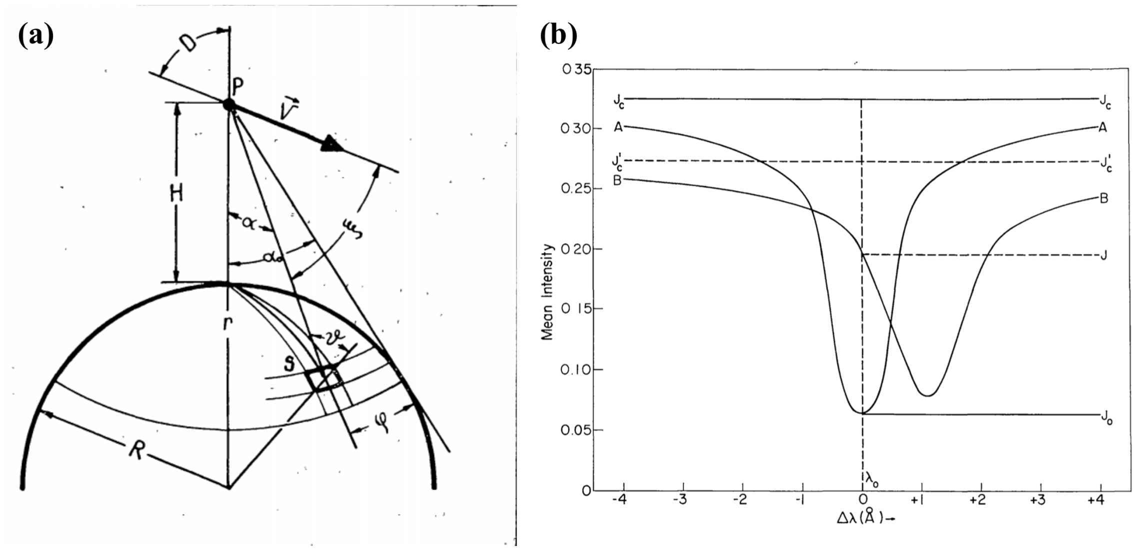

Figure 3.8: (a) Geometry of Doppler dimming. The large circle at the bottom represents the sun, the point P represents the position of mass that has erupted e.g., a CME. The vector V is the velocity of the CME. The square patch on the sun represents an area of source emission. Adapted from Rompolt (1967). (b) The Hα profiles seen by (A) a stationary observer at a height of 5600 km above the photosphere; and (B) an observer at a height of 30,000 km moving radially outward at 75 $km\ s^{-1}$. The mean intensity (as seen by the scattering medium) is measured in units of the intensity of the nearby continuum at the center of the disk. It can be seen that the Doppler shift also causes an intensity decrease. Adapted from Hyder and Lites (1970).

The second type of dimming that results from a Doppler effect is one we call "bandpass dimming". This physical process is tied to the observers location similarly to obscuration dimming (see Section 3.5). Mass ejected toward the observer will have emissions that are necessarily blue-shifted. If the velocity is high enough, it can shift emission lines outside of an imager's bandpass, causing an apparent dimming in the data. Most imagers use filters that tend to have bandpasses on the order of nanometers but can have sharp edges (Figure 3.9). CMEs typically have speeds ranging from a few hundred to a couple thousand $km\ s^{-1}$. However, a CME only accounts for a small fraction of the total emission from the solar disk. As noted in Hudson et al. (2011), these Doppler shifts tend to be on the order of picometers. Additionally, a CME moving fast enough to shift emission outside the bandpass would be outside the field-of-view of the instrument in a very short time. Thus, this type of apparent dimming is not expected in EUV images, but we include it for completeness and note that this may be a consideration for designing future instruments.

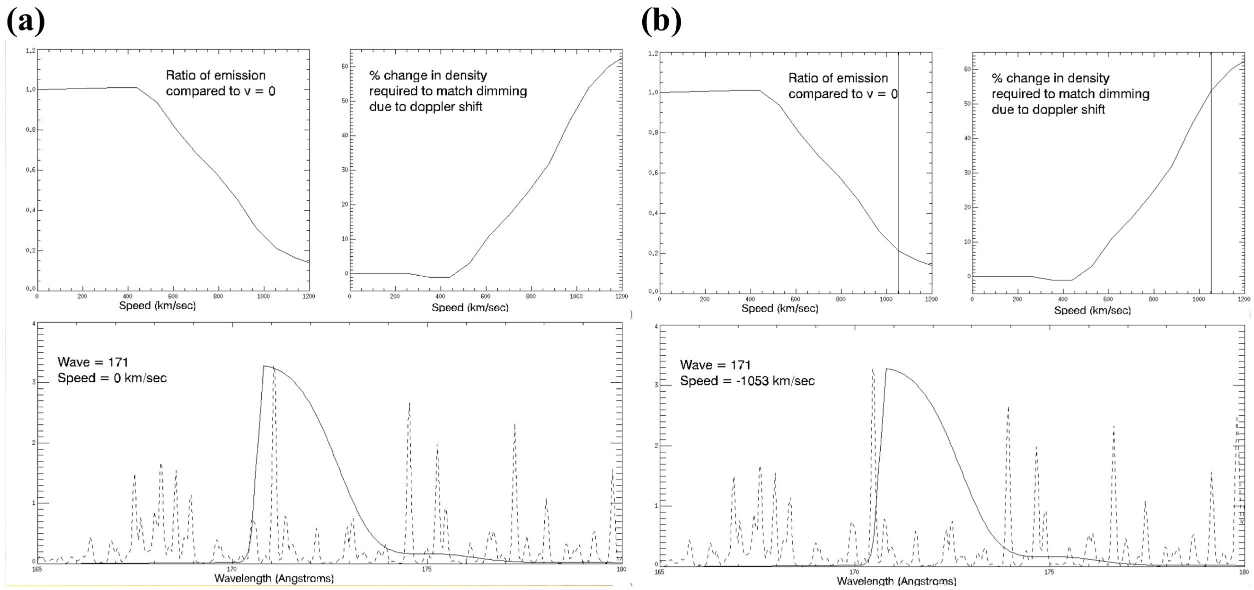

Figure 3.9: Spectra to illustrate bandpass dimming, taken as snapshots from a movie produced by Barbara Thompson. (a) Bottom: The dashed line shows a modeled solar spectrum and the solid line shows the bandpass for AIA's 171 Å. Top left: The ratio of emission relative to plasma with no line-of-sight velocity as a function of velocity. Top right: The amount of density decrease (in %) that would be required to achieve the same amount of dimming as bandpass dimming at each velocity. (b) Same as (a) but at a velocity of 1053 $km\ s^{-1}$, which is an example of the 171 Å emission Doppler shifting outside the associated AIA bandpass.

In a spectrograph like EVE, the Doppler shifts would instead simply cause a wavelength shift of the emission line from the ejected material, which is how Hudson et al. (2011) performed their Doppler analysis of the EVE datas. When this Doppler-shifted emission is convolved with the relatively static plasma remaining on the sun, a small Doppler shift from the ejected material manifests as line-broadening in the integrated irradiance while a large shift would result in a line splitting. It should be noted that the EVE extracted lines data product applies a static mask to the spectra so a sufficiently large Doppler shift could cause an apparent dimming in this product. Again, the observed shifts are far too small to impact the EVE data analysis.

3.6 Dimming Physics and Observations Summary

The physics for most of these types of dimming is relatively simple and well-understood, with the exception of global waves. Mass-loss dimming is simply the direct result of a CME removing a significant quantity of emitting material from the solar corona. The coronal dimming amount increases as the CME pulls away, reaches a maximum dimming depth, and then the emission begins to return to the original pre-flare level after a few hours as post-flare loops begin to replace the lost plasma from the surrounding corona and transition region. Instrumentally, even though EUV measurements select specific temperature ranges, mass-estimates based on them appear consistent with white-light coronagraph derived masses (Aschwanden et al., 2009a).

Thermal dimming is a major concern in nearly all of the citations above for its potential to interfere with mass-loss dimming analysis and the resultant estimated CME masses. The physics here is also simple: eruptive events result in various forms of heating (see Section **??**) that shift upward the ionization fraction of dominant EUV emitters (e.g., Fe). Instrumentally, this effect can be compensated for by measuring emission lines from multiple ionization states of the same ion (e.g., Fe IX-XV).

Obscuration dimming physics are also simple, essentially a result of Beer's law, as light passes through a medium with nonzero opacity. Instrumentally, this is easily identified with imagers and we believe it may be possible to identify with a spectrograph, provided some chromospheric helium emission lines are measured (e.g., 256 Å and/or 304 Å).

The physics of global waves is highly contested but the observations are well established. For a disk-integrating spectrograph like EVE, which is the primary source of data analysis herein, we believe that wave dimming will be negated by wave brightening. Indeed, to our knowledge, no observations of waves have been detected from EVE observations.

Doppler dimming physics are well understood and long standing. A CME may fluoresce due to stimulation from the sun, but the wavelengths will be Doppler shifted according to the relative velocity of the CME from the sun. This shift reduces the efficacy of the stimulation, resulting in less fluorescence. However, the dimming region in this case is the CME itself, which is likely to be outside the field of view of instruments like AIA and EVE. Additionally, the emission lines of interest in this study are collisionally dominated. Thus Doppler dimming is an interesting phenomenon but is not expected to dramatically impact analyses of the other types of dimming.

The physics of bandpass dimming is simple Doppler shifting of an emitting plasma. Potential dimming in this case is primarily an instrumental effect, as the Doppler shift could push important emission lines outside the instruments bandpass or data processing line-selection masks. However, studies have shown that the actual Doppler shifts are orders of magnitude too small to cause this type of dimming.

Chapter 4

Coronal Dimming Case Studies

This chapter focuses on the detailed analysis of two coronal dimming events. One was selected for its relative simplicity, involving only mass-loss dimming and some thermal effects, while the other was selected for its complexity, involving nearly all of the types of dimming as described in Chapter 3. Observations and analysis of the EUV irradiance and images of these events as well as the related coronagraphs are first described in Section 4.1. A new method for deconvolving flare emission from dimming irradiance measurements is developed in Section 4.2 while Section 4.3 contains the associated error propagation. Finally, Section 4.4 provides analyses spanning the observations of these two coronal dimming events and parameterizes dimming into depth and slope. We find that the new deconvolution method for irradiance successfully matches the dimming profile extracted from the spatially-isolated dimming as obtained from EUV image time series for the simpler dimming case. Thus, we show that it is possible to accurately characterize dimming in a localized area even with no spatial resolution. Further analysis of the complex dimming will be required to isolate mass-loss from the full-range of cotemporal dimming processes, which will be a topic of postdoctoral research. The preliminary analyses of this more complex dimming are provided here.

4.1 Observations and Analysis

4.1.1 Simple Dimming Case

This event occurred on 2010 August 7 at approximately 18:24 UT. The eruptive event consisted of an M1.0 flare, dimming in the region around the flare, and a coronal mass ejection (CME). Other, relatively distant, active regions were also on disk but did not have any significant sympathetic responses. Mass-loss dimming and flare-related thermal effects were found to be important, while the other type of dimming (see Chapter 3) were negligible.

Coronagraph Observations

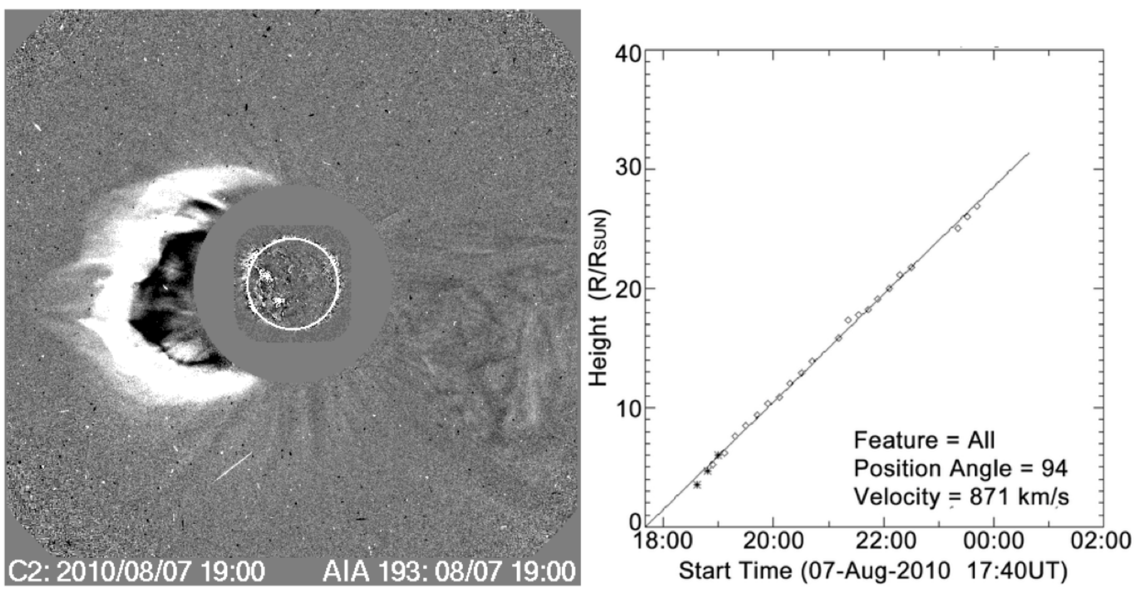

Figure 4.1: CME event at 19:00 on 2010 August 7. Left: difference image from LASCO C2 and AIA 193 Å channel. Right: CME height versus time shows nearly linear velocity of 871 $km\ s^{-1}$. Figure adapted from CDAW CME Catalog, courtesy of S. Yashiro and N. Gopalswamy.

The Coordinated Data Analysis Workshops (CDAW) LASCO CME catalog (herein referred to simply as the CDAW catalog) is an extensive database of all CMEs observed by the SOHO/LASCO coronagraphs with related quantities such as date, time, computed velocity, and sometimes mass (Gopalswamy et al., 2009). The CDAW catalog has seven CME events listed for 2010 August 7. All but two of them occur prior to the M1.0 flare at 18:24 UT that is of primary interest for the present study. This rules out all but those two to be CMEs associated with the M1.0 flare. The CME shown in Figure 4.1 is flagged as a halo event with a time of 18:36 UT in CDAW, while the next event occurred with a central position angle of 116° at 22:24 UT. The timing and location of the flare and associated dimming region suggest that the halo CME is the one associated with the dimming. The plane-of-sky velocity estimate for this CME is 871 $km\ s^{-1}$ as indicated in Figure 4.1. No mass is listed for this CME in CDAW, but using LASCO and STEREO data and the techniques outlined in Colaninno and Vourlidas (2009), a mass of 6.4×10^{15} g was computed for this CME event (A. Vourlidas 2014, private communication). A true space velocity was also computed as 850 $km\ s^{-1}$ at 9 R$\odot$ with a deceleration of 6.84 $m\ s^{-2}$ (Figure 4.2). Based on these estimates for mass and velocity, this CME is considered be of modest size.

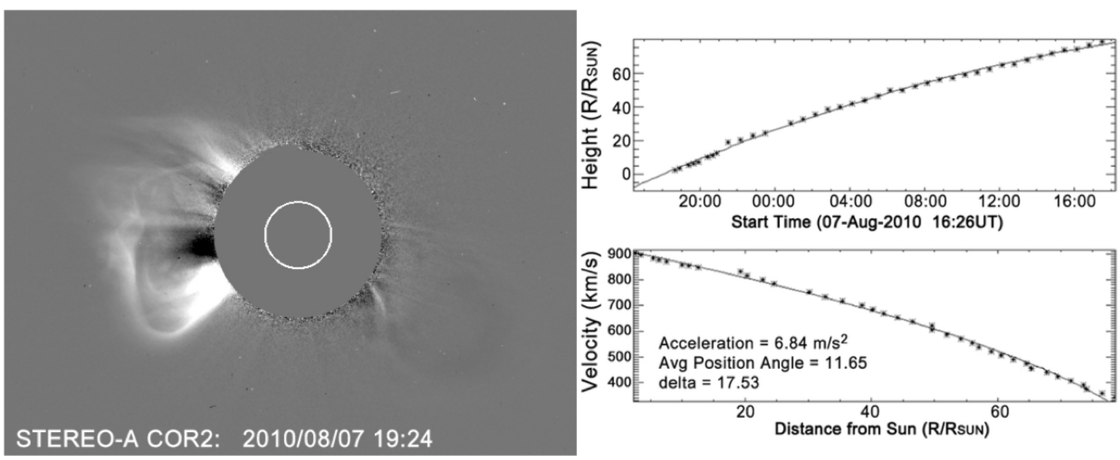

Figure 4.2: Left: STEREO-A COR2 difference image at 19:24 UT. Right: CME height vs. time calculated from STEREO and shows a deceleration of 6.84 $m\ s^{-2}$. Figure courtesy of Barbara Thompson.

SDO/AIA EUV Image Observations The relative simplicity of this event is why it was chosen for a case study. The observations in AIA do not suggest that obscuration, waves, or Doppler shift contributed to the observed dimming. The area in the red contour of Figure 4.3 was selected manually (by eye) to represent the region of mass loss. Pixel values inside each contour were summed and a time series of these sums created with successive images in multiple AIA wavelength bands. These light curves are shown on the right of Figure 4.3. The light curve for the red contour shows clear dimming in 193 Å and 171 Å. In fact, the dimming from this region accounts for nearly all of the observed dimming throughout the entire event. This contour was selected after several iterations that indicated slight deviations in the contour had minimal impact on the light curve, as long as the dark region was fully encompassed. In other words, the result is fairly insensitive to the precise contour selection. The other contours were also selected manually to isolate regions of potential dimming e.g., as a sympathetic response from the solar eruptive event of interest. The exception is the magenta contour surrounding the flare loops that brightens dramatically but does not ever dim.

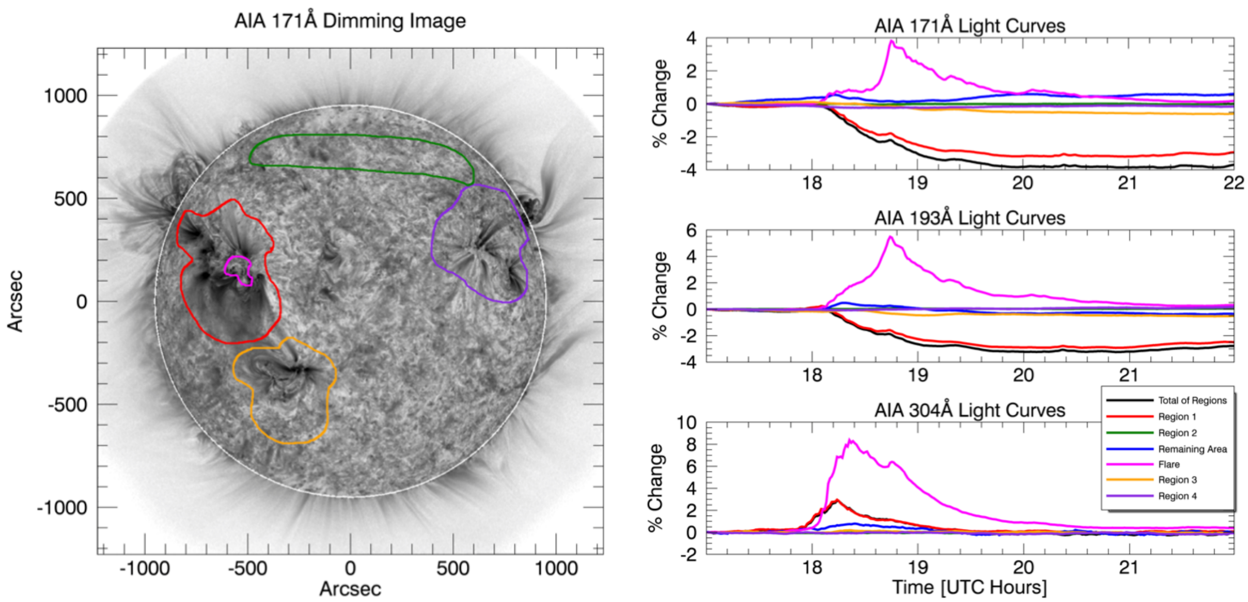

Figure 4.3: AIA results for the M1.0 Flare on 2010 August 7. Images improved by using point spread function to compensate for instrument "blurring" of light. Left: AIA 171 Å channel difference image with subjectively selected region contours overlaid. The red contour outlines what is thought to be the region of mass loss. The orange and purple contours outline other active regions on the disk, which have the potential to have sympathetic dimming. The green contour outlines a filament, which also has the potential to sympathetically dim based on its behavior during the M flare on 2010 August 5. The magenta contour isolates the flaring coronal loops. The white line around the solar limb is an artifact of the solarsoft derotation method. Right three plots: light curves of AIA 171 Å, 193 Å, and 304 Å channels for the color-corresponding contours on the AIA image. The blue line is the light curve for all on-disk area not enclosed by a contour. The black line is the sum of all contoured regions and acts as a proxy for total dimming. All percent changes are calculated from the band's value at 17:00 UT, prior to the flare. The transition region He 304 Å emission does not show dimming; both corona Fe emissions (171 Å and 193 Å) show dimming.

The He II 304 Å light curves are included to provide a contrast to the dimming effects seen in the coronal Fe lines. This He II wavelength is generated primarily in the chromosphere and transition region, as opposed to the coronal source of the other wavelengths. Mass loss occurs primarily in the corona, as the term coronal mass ejection suggests. This is reflected in the lack of dimming observed in the non-coronal He II 304 Å emission line.

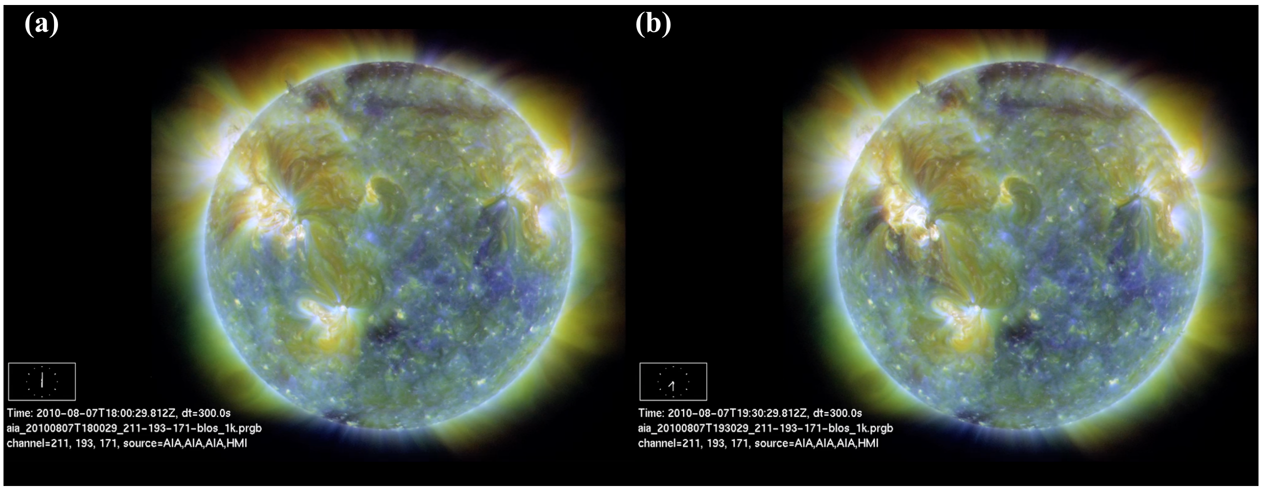

Figure 4.4: AIA composite images (a) prior to solar eruptive event and (b) during deep dimming. In these images, purple is 211 Å, brownish-gold is 193 Å, and yellow is 171 Å. These static images show dimming in the region as outlined in Figure 4.3, though the change is much more dramatic and obvious when viewed as a movie.

Thermal effects may play a role in this event but may be difficult to quantify using only AIA because the relatively wide spectral bands of AIA channels mean many emission lines and continuum are blended together (see Figure 2.1 and Table 2.1), which makes specifying a well-defined temperature difficult. Nevertheless, some indication of temperature is given by AIA and multi-wavelength composites can aid in this analysis. Figure 4.4 shows AIA composite images (211 & 193 & 171 Å) before the solar eruptive event and during the dimming. All of these bands correspond primarily to the corona and transition region. If an area is dark, that means that there is little emission in all three of these wavelengths. Since these three bands span temperatures across at least 0.6-1.86 MK, that is indicative of mass loss. In areas where temperature effects are very strong, e.g., heating in the confined flare loops, it can be seen that emission is strong in all three of these bands resulting in the composite being white. Even though the flare loop region is also where the highest ionization states and their emission can be found, there is still ample emission in these relatively low ionization states of Fe. Thus, it's unlikely that a region in these composites would become dark purely from a temperature change. EVE is less sensitive than AIA to blending in temperature space due to its higher spectral resolution and plethora of emission lines from Fe at different ionization states. A future study using the differential emission measure techniques of Caspi et al. (2014) to study the temperature evolution could help to quantify this effect.

SDO/EVE EUV Irradiance Observations Figure 4.5 shows a trend that is consistent with the findings from Figure 3.4 –that an ion's peak formation temperature[1] is inversely proportional to magnitude of dimming. The transition from an ionization state that shows dimming to ones that only show brightening occurs at Fe XIV 211 Å, which itself shows dimming in some events but not others. The transition for where the Fe emission shows dimming varies by solar eruptive event. For example, the Fe XVI 335 Å emission has shown dimming for larger CME events (Woods et al., 2011). Herein, we will refer to Fe IX 171 Å through Fe XIV 211 Å as "dimming lines" and Fe XIV 211 Å through Fe XXIV 192 Å as "nondimming lines" (note that 211 Å is included in both descriptions to reflect its ambiguity).

It is also important to note in Figure 4.5 that the onset of dimming in the dimming lines is nearly simultaneous. Meanwhile, the gradual-phase flare peak is delayed in lower ionizations of Fe, which is due to a cooling effect. The primary source of energy release in a flare is near the point of magnetic reconnection, typically far above the footpoints of the magnetic loops involved, in the corona. Some of the energy goes into the acceleration of particles downward. When these particles impact the denser chromosphere, they cause the heating and chromospheric evaporation. As that thermal plasma enters the corona it cools (Fletcher et al., 2011), and highly ionized Fe gains electrons. Thus, the peak is later for lower ionization states in this case as seen in Figure 4.5. The Fe IX 171 Å irradiance, in particular, shows the competing effects of this gradual phase flare

[1] Recall that greater ionization requires greater energy and that temperature is one measure of energy content for a Maxwellian plasma

peak and coronal dimming: it's irradiance begins to drop at the same onset as the other emission lines, then has a positive peak of about +2%, and drops to a dimmed condition again. Images with spatial resolution can isolate the flaring region responsible for this peak, as is shown with the magenta contour in Figure 4.3. Alternatively, we have developed a method for isolating and removing this peak in dimming lines with the spatially-integrated irradiance from EVE, which will be detailed in Section 4.2.

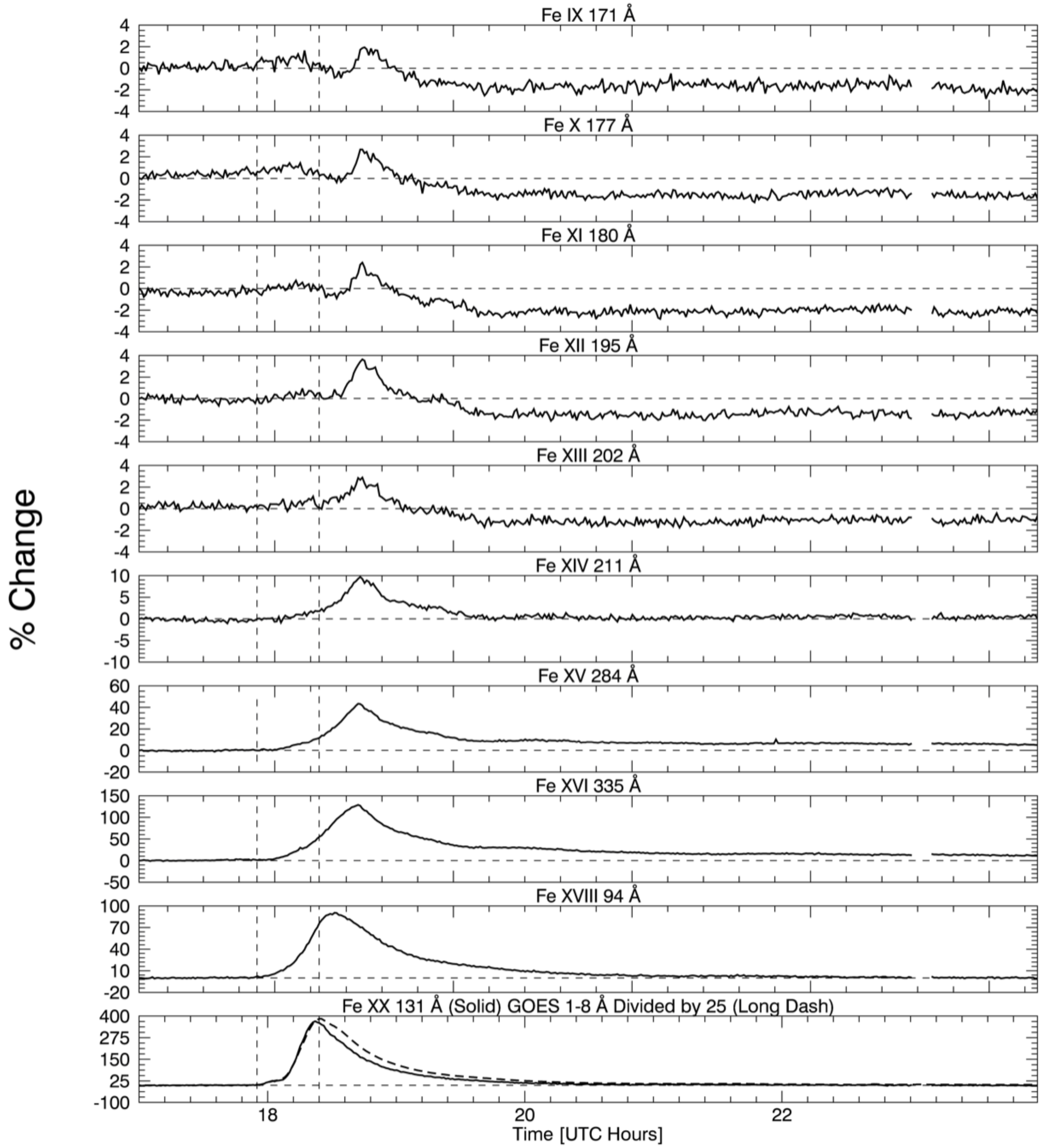

Figure 4.5: One minute average EVE light curves of the 2010 August 7 coronal dimming event for most of the spectral lines listed in Table 2.1, as well as the GOES 1-8 Å channel light curve. The leftmost vertical dashed line indicates the GOES event start time, while the other vertical dashed line indicates the GOES event peak time. Peak formation temperature of the EVE spectral lines increases from top to bottom plot. Fe IX to Fe XIII show clear dimming, Fe XIV is borderline, and Fe XV to Fe XX show smooth brightening with no dimming. The Fe XX 131 Å profile is very similar to GOES 1-8 Å, indicating that this line in EVE is a good proxy for gradual phase timing. Also note the vertical axes: dimming is on the order of a few percent for the cooler Fe emissions while the hotter Fe emissions have bright peaks in the hundreds of percent. All percent changes are calculated from the spectral irradiance at 17:00 UT.

4.1.2 Complex Dimming Case

This event occurred on 2011 August 4 at approximately 3:47 UT. It spawned from NOAA active region 11261 at location N19W36. The eruptive event consisted of an M9.3 flare, a large and fast CME, and nearly all of the types of dimming discussed in Chapter 3: mass-loss and thermal dimming, a global wave that then triggered a sympathetic filament eruption, and an obscuration dimming from the filament. No bandpass or Doppler dimming were identified even in this relatively energetic event. This event was chosen specifically for presenting so many types of dimming and related physical processes in a single case.

Coronagraph Observations

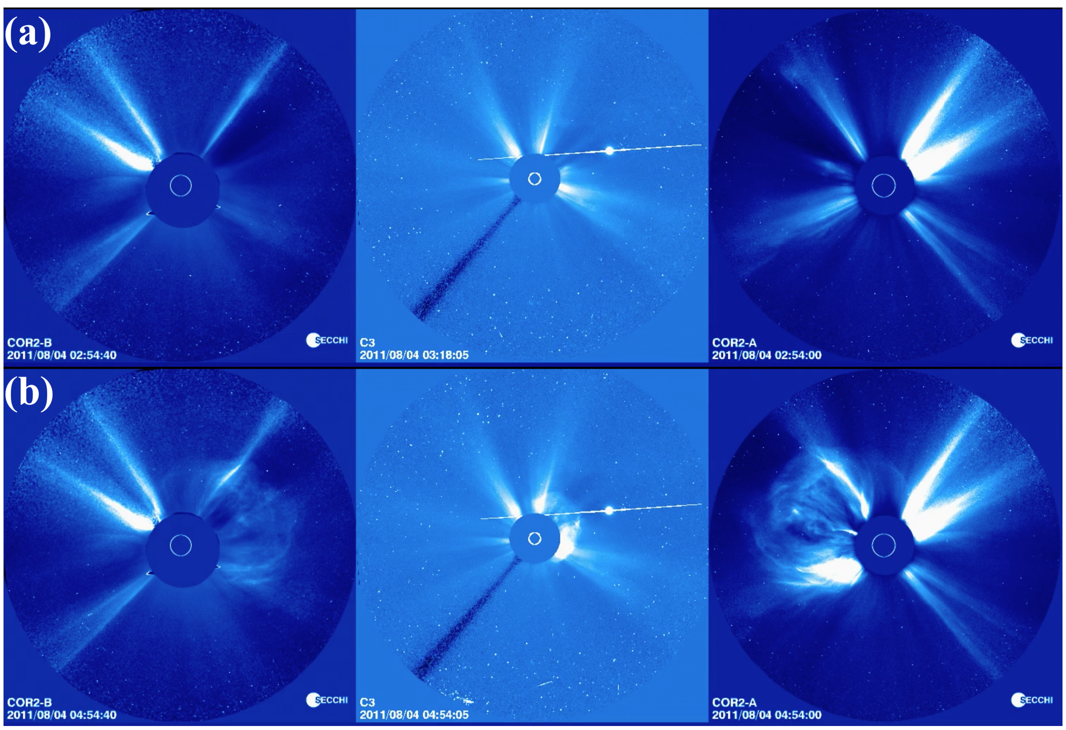

Figure 4.6: Coronagraph images of CME associated with 2011 August 4 dimming event. From left to right the coronagraphs are STEREO Behind C2, LASCO C3, and STEREO Ahead C2. Top: Images prior to CME. Bottom: Images during CME.

Images from the three coronagraphs are shown in Figure 4.6. The CME in Figure 4.6 (b) can be seen in STEREO-B (behind) on the right of the solar disk, in LASCO as the start of a halo CME offset to the upper-right of the disk, and in STEREO-A (ahead) on the left of the disk. Additionally, bright streamers can be seen inside the CME and on the opposite side of the Sun, signifying that the outer corona of the Sun was also in a more complex configuration than the 2010 August 7 case.

The CDAW catalog for this event lists it as a halo CME with a velocity of 1315 $km\ s^{-1}$, relatively fast for a CME (faster than 99.03% of other CMEs, see Figure 4.7), and a mass of $1.16 \times 10^{16}\ g$. However, halo CMEs present a strong challenge for obtaining accurate mass, and the catalog flags it as a poor mass estimate. Mass estimates based on the three coronagraphs are $8.6 \times 10^{15}\ g$ for LASCO C3 (35% lower than the CDAW value), $7 - 8 \times 10^{15}\ g$ for STEREO-A COR2, and $4.3 \times 10^{15}\ g$ for STEREO-B COR2 (A. Vourlidas 2013, private communication). A deprojected, 3-D analysis has not been performed for this CME.

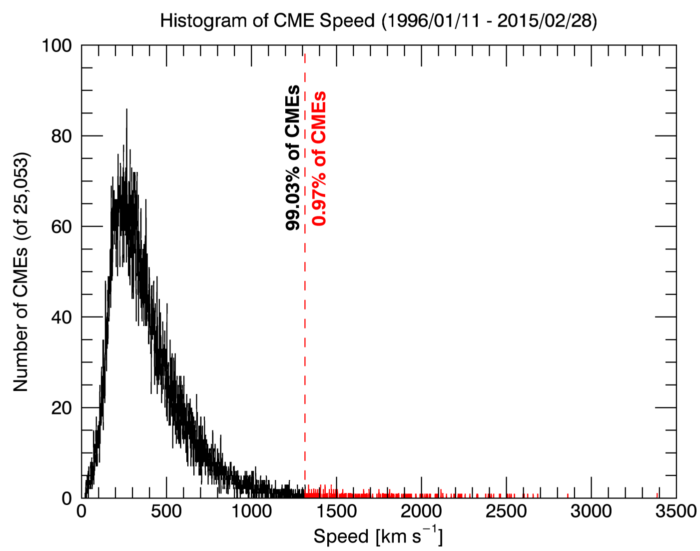

Figure 4.7: Histogram of CME speed from 1995 to 2015 based on the CDAW LASCO CME catalog's 25,053 CMEs with listed speeds. The red vertical line is at 1315 $km\ s^{-1}$, the listed speed of the 2011 August 4 event.

SDO/AIA EUV Image Observations

The complexities of this eruptive event are quite apparent in AIA observations. Figure 4.8 is

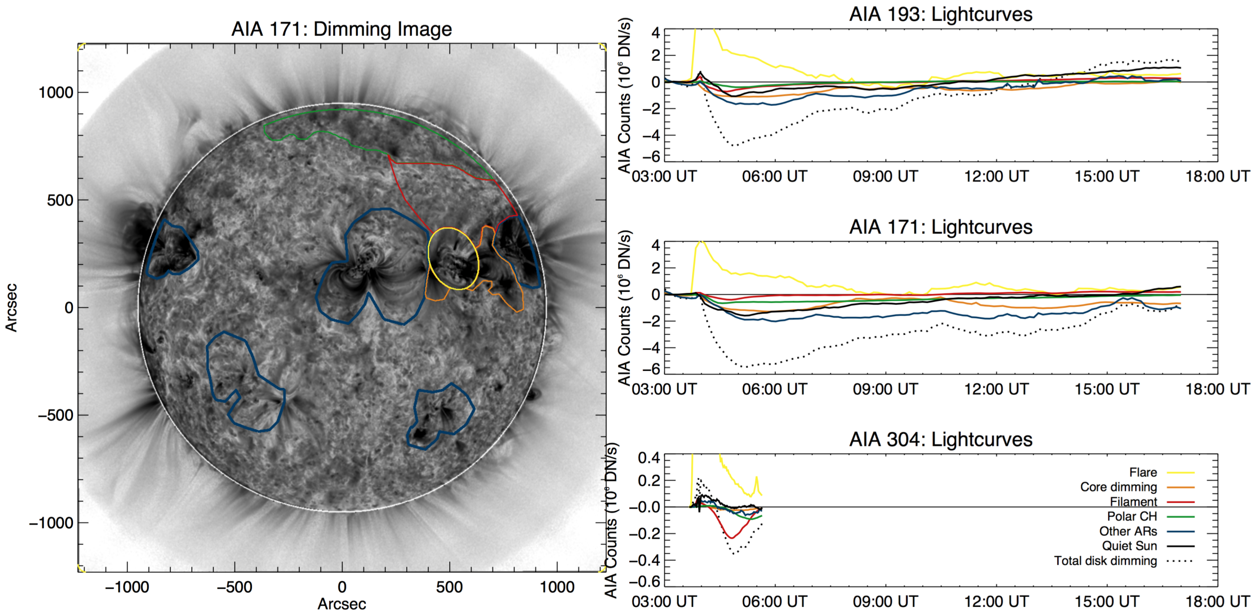

Figure 4.8: Same as Figure 4.3 but for 2010 August 7 event. Colored contours and lines in plots correspond according to legend, but are different from Figure 4.3. An additional difference is that the He II 304 Å line now shows dimming. Not all 304 Å data were available at the time of processing, which is why the time series ends at 6:00 UT. Figure courtesy of Rachel Hock.

in the same format as Figure 4.3 but is for the 2011 August 4 event. Dimming is seen in numerous locations for this event, indicating the far-reaching influence of this eruption. In particular, even though 304 Å data were not processed to the end of the dimming window[2] , the main phase of obscuration dimming is clearly visible. Additionally, 193 Å and 171 Å show dimming in every region outside of the flare-isolating contour (yellow). The primary region thought to be associated with mass-loss dimming is labeled "core dimming" (orange) here. It corresponds to an area immediately surrounding the active region where the flare took place and is bounded by quiet-Sun on top and bottom and other active region loops to the left and right. All other active regions visible on disk are contained in blue contours and eventually show even greater dimming than the core region (orange). Note that for the first several minutes, the core dimming dominates the other active regions. Also, the dotted black dash line is the disk signal excluding the flare region (yellow),

[2] Figure 4.9 shows these data in full, though for differently selected contours

effectively the sum of all plotted lines except yellow. It can be seen that the relative contribution of each region to the total dimming is nonzero. Table 4.1 details these contributions.

The overall structure of Table 4.1 is wavelength and feature (vertical) and contribution at maximum dimming (i.e. minimum count), maximum dimming contribution, and the range of contributions. It can be seen that in 193 Å and 171 Å, peak dimming is dominated by the non-flaring active regions. As will be shown later, this is mainly a reflection of the most nearby active region's dimming. It is also worth noting that core dimming reaches its maximum dimming 36 minutes earlier than non-flaring active regions. This suggests that the latter is either a sympathetic response to the primary dimming catalyzed by the global wave or additional mass being ejected that becomes the tail side of the CME. As expected, in 304 Å, the minimum count is dominated by the filament (red). This is consistent with the physical theory for obscuration dimming detailed in Section 3.5. The dominant region changes when looking at the maximum contribution. Here, core dimming dominates for 193 Å but the non-flaring active regions still dominate in 171 Å. Again, we will soon show that the most nearby active region contributes greatly to the dimming and may have contributed to the outgoing mass of the CME. 304 Å remains consistent for contribution maximum, with its greatest value coming from the filament eruption. Finally, the range of contributions shows that in 193 Å, core dimming and non-flaring active regions are comparable in their dominance; 171 Åhas greater contribution from non-flaring active regions and the quiet-Sun; and 304 Å is very clearly dominated by the filament.

Figure 4.9 is the same format as Figure 4.8 but with different regions selected, and does not use images corrected with the point spread function. The latter explains why the total dimming is about 2% less than in Figure 4.8. Of importance here is that the red contour, which encompasses the core dimming region from Figure 4.8 and the most nearby non-flaring active region, accounts for the majority of total dimming in 193 Å and 171 Å. These two active regions are so close together that it is possible that the CME pulled mass away from a coronal volume encompassing both active regions. It can also be seen that 171 Å has a more prominent dimming in the remaining area (blue), i.e. quiet-Sun, than in 193 Å. This is evidence of heat-wave dimming described in Robbrecht and

Table 4.1: Statistics for dimming features in Figure 4.8 for 2011 August 4 event. Table courtesy of Rachel Hock.

Dimming Feature	Count Minimum			Contribution Maximum			Range of Contribution (%)
	Time (UT)	Counts (10^6 DN s^{-1})	Contribution (%)	Time (UT)	Counts (10^6 DN s^{-1})	Contribution (%)	
AIA 193:							
Total disk dimming	4:55	-4.81					-
Core dimming	5:17	-1.11	25.3	04:05	-0.63	73.1	18.9- 73.1
Filament eruption	4:41	-0.72	16.2	04:05	-0.23	27.2	1.0- 27.2
Polar coronal hole	5:03	-0.39	8.5	05:17	-0.38	8.7	0.6- 8.7
Non-flaring active regions	5:53	-1.72	43.1	08:04	-1.05	54.6	29.6- 54.6
Quiet Sun	4:55	-1.07	22.3	08:40	-0.57	26.0	8.0- 26.0
AIA 171:							
Total disk dimming	5:10	-5.46					-
Core dimming	5:53	-1.28	24.5	04:05	-0.40	27.3	9.4- 27.3
Filament eruption	4:48	-0.40	8.0	04:41	-0.38	8.1	0.0- 8.1
Polar coronal hole	4:34	-0.66	15.7	04:26	-0.63	16.6	7.5- 16.6
Non-flaring active regions	6:00	-2.02	38.9	08:54	-1.72	53.9	16.6- 53.9
Quiet Sun	5:10	-1.59	29.0	04:05	-0.68	46.7	20.8- 46.7
AIA 304:							
Total disk dimming	4:53	-0.36					-
Core dimming	5:08	-0.03	9.5	04:23	-0.02	62.2	7.4- 62.2
Filament eruption	4:49	-0.24	69.4	04:25	-0.08	304.3	9.4- 304.3
Polar coronal hole	5:22	-0.09	40.0	05:38	-0.06	49.3	1.1- 49.3
Non-flaring active regions	5:11	-0.06	20.6	05:31	-0.05	25.1	2.4- 25.1
Quiet Sun	5:34	-0.02	14.0	05:37	-0.02	14.4	0.1- 14.4

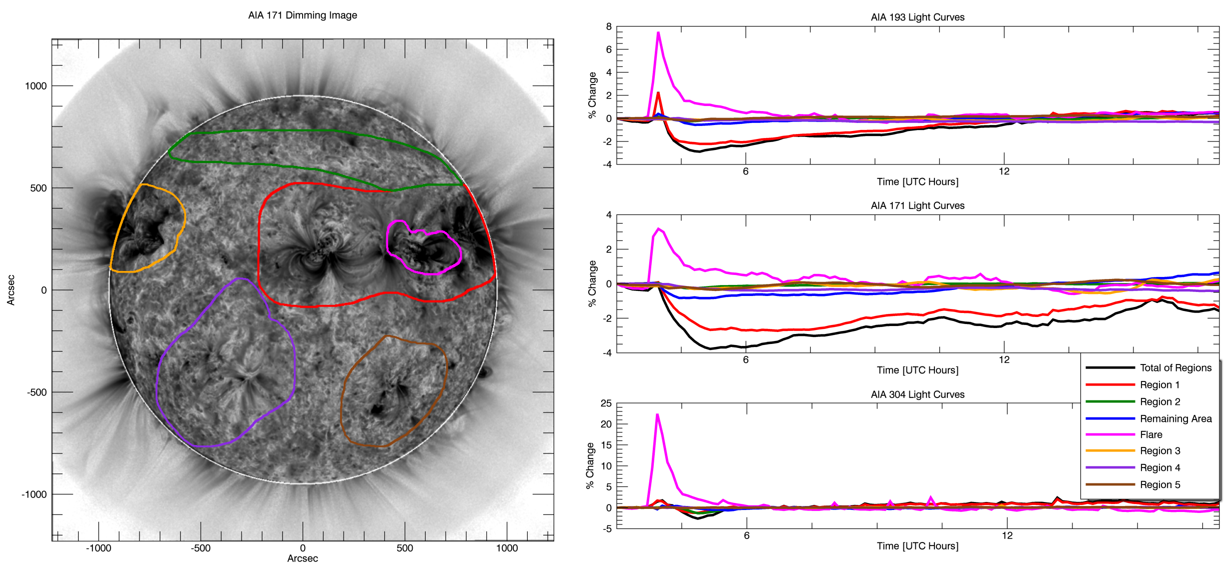

Figure 4.9: Same as Figure 4.8 but with new contours selected and no point spread function correction applied. Also 304 Å data are now complete.

Wang (2010).

Also note that while the AIA 193 Å band contains the Fe XXIV 192 Å emission line, this high ionization state is only expected in hot plasma such as in flaring loops, which are spatially isolated in the contours of Figures 4.3, 4.8, and 4.9. Thus, for this particular case of spectral blending, the impact on analysis and interpretation is minimized.

Running-difference movies make viewing EUV waves easier but it is difficult get the same clarity with static images. Instead, Figure 4.10 follows a similar format to earlier AIA figures but draws geometric contours propagating from the source active region. The light curves in Figure 4.10 are color coded from dark to light corresponding to increasing distance from the source region. The propagation of the wave can be seen as the dark curves reach their minimum earlier with larger magnitude and the lightest curves show only a minor impact from the wave. This is expected behavior for any impulsive wave phenomenon as energy is dissipated in the surrounding medium.

SDO/EVE EUV Irradiance Observations Figure 4.11 shows selected extracted emis-

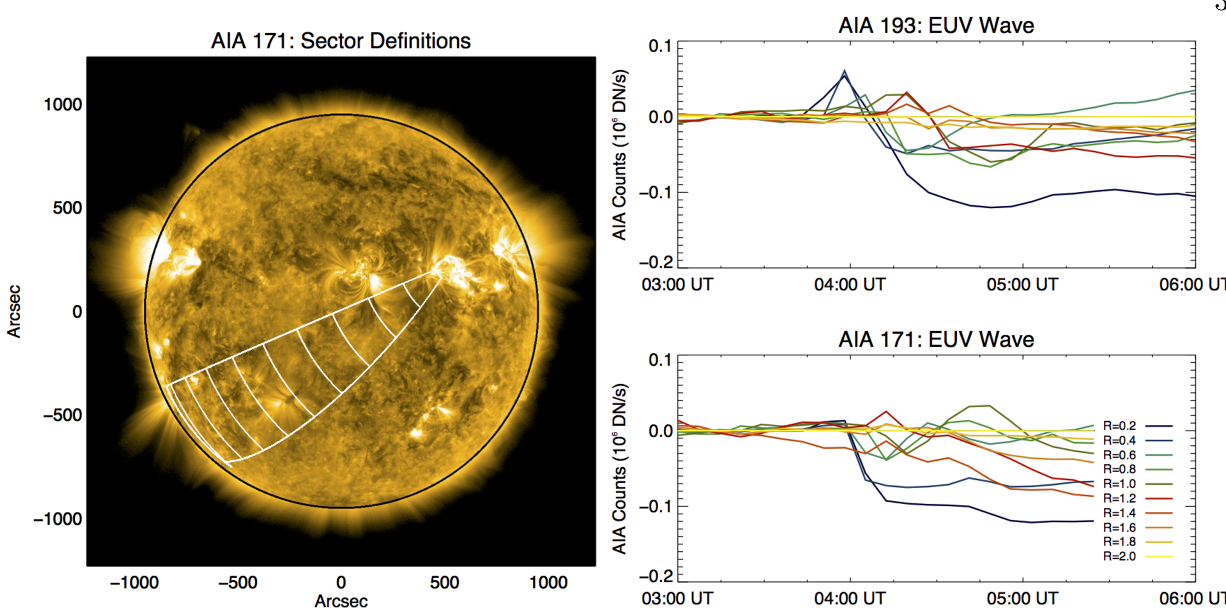

Figure 4.10: Similar format to Figure 4.9, but with geometric contours selected specifically for analysis of propagating wave. In the line plots on the right, distance from the source active region increases with lightness of color. Figure courtesy of Rachel Hock.

sion lines from EVE for the 2011 August 7 complex eruptive event. Because obscuration dimming is important for this case, the plot includes two He II lines: 256 Å and 304 Å, both of which show dimming at approximately the same time as what was seen in AIA (Figure 4.8). The irradiance increase from roughly 5:00 to 7:00 UT in Fe XIV 211 Å may relate to the EUV late phase discussed in Woods et al. (2011). Dimming in Fe IX to Fe XIII was significant in this case, roughly twice as large as in the simpler 2010 August 7 event. Furthermore, the peak time versus ionization state trend is reversed compared to the simpler event e.g., Fe IX 171 Å actually peaks just prior to the GOES event peak time (second vertical dash), and higher ionization states peak later and later. This is indicative that heating processes are dominating the overall irradiance. In either heating or cooling cases, the flare-dimming deconvolution method discussed in Section 4.2 works equally well.

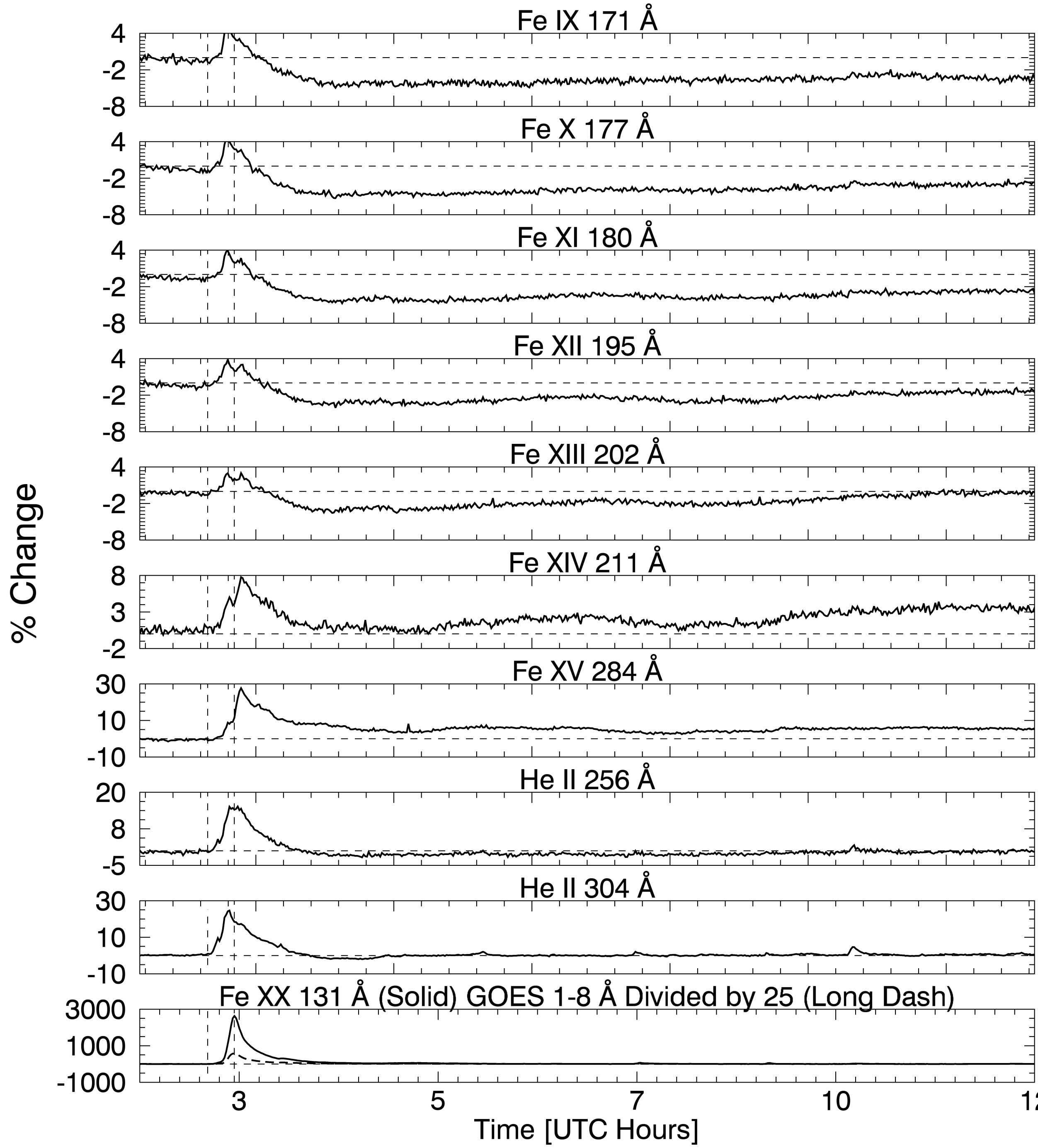

Figure 4.11: Same as Figure 4.5 but for the 2011 August 4 event, and showing He II 256 Å and 304 Å instead of Fe XVI 335 Å and Fe XVIII 94 Å. Just as before, Fe IX to Fe XIII show clear dimming, Fe XIV is borderline, and Fe XV to Fe XX show smooth brightening with no dimming. The Fe XX 131 Å profile is 3x larger than GOES 1-8 Å but still has a similar shape and timing. Also note the vertical axes: dimming is 2x larger than it was for the 2010 August 7 event. The two He II lines show dimming as well, suggestive of obscuration dimming.

4.2 Flare-Dimming Deconvolution Method

Figures 4.5 and 4.11 showed how cooling and heating impact the time of an irradiance peak in each ionization state of Fe: cooling causes the low ionization states to peak later and heating causes the reverse. In either case, it is clear that dimming magnitude decreases with higher ionization states of Fe. Eventually, around Fe XIV at 211 Å, dimming is no longer clear. The next ionization state, Fe XV at 284 Å, shows strong brightening in response to the flare but no dimming. The shape of the flare peak is similar in all wavelengths[3] . Using this observation, we developed a simple algorithm to remove the flare peak in the dimming lines. We make the assumption that the peak in the high ionization states is a good proxy for what *would have* been observed in the low ionization states if there were no dimming. However, the magnitudes and timing are quite different. To account for this, we scale the larger peak down and shift it in time so that they are matched. An example of the process is shown in Figure 4.12 and a flow-chart of the algorithm is shown in Figure 4.13. The ten-second EVE data are averaged to two-minutes to reduce noise (see black line in Figure 4.12) and the simple IDL *max* function applied to find the peak in the light curve for every emission line listed in Table 2.1. Then, the scaled non-dimming emission line is shifted in time such that its peak matches the one in the dimming line (see green line in Figure 4.12). Finally, the scaled and time-shifted non-dimming light curve is subtracted from the dimming emission line (see blue line in Figure 4.12).

The red line in Figure 4.12 is the same red line that was in Figure 4.3, which corresponded to the dimming area in AIA thought to be most associated with mass-loss from the corresponding observed CME. It is clear that the deconvolution method applied brings the EVE light curve much closer (from black line to blue line) to the AIA one (red line). The agreement is not perfect, particularly at later times, and the noise in EVE is greater – even with the two-minute averaging – than AIA. However, the agreement during the initial decline is much better and is where the slope of dimming is computed, which will be shown to be a critical proxy to CME velocity. The later rise

[3] Though the shape of the flare peak appears to become more smooth at higher ionization states because of the significantly larger increase making the small oscillations imperceptible in the plots

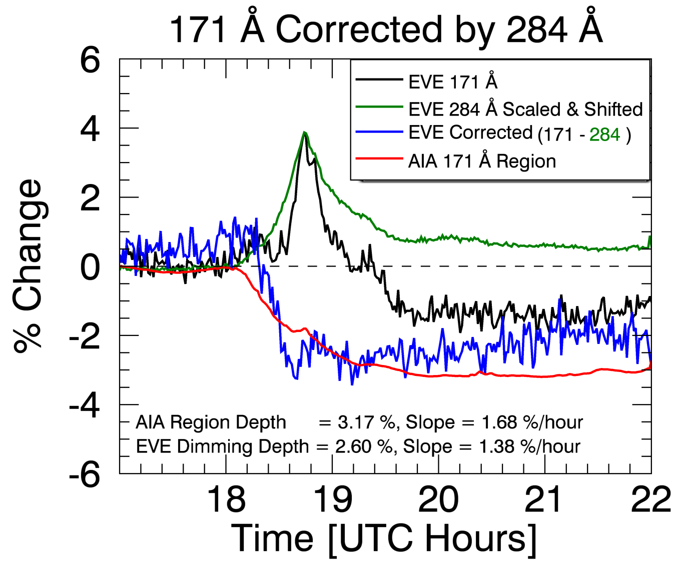

Figure 4.12: Example of the flare-dimming deconvolution method. This particular event is the simple case described in Section 4.1.1. A non-dimming line (e.g., 284 Å) is scaled down and shifted in time such that its flare peak matches the one in a dimming line (green and black, respectively). The scaled and time-shifted non-dimming light curve is then subtracted from the dimming light curve, resulting in a "corrected" or "deconvolved" light curve representative of mass-loss dimming (blue). The red line is the same as the red line in Figure 4.3, indicating the spatially isolated dimming in AIA 171. Dimming depth and slope are shown at the bottom of the plot and were computed at a particular time and time range, respectively.

in the corrected EVE line (blue) is due to a slow decrease in the scaled & time-shifted correction line (green). The unaltered dimming line (black) is relatively flat in the later hours of the dimming, consistent with the AIA light curve (red). This behavior varies by event but a “bottomed-out” dimming is common. Typically, the maximum depth is reached quickly and maintained for several hours. It will later be shown that depth is another critical proxy for CMEs; this one for CME mass. In practice, the depth is measured at a point soon after the maximum dimming is reached, so later behavior of the corrected EVE line (blue) is of less importance than the removal of the flare peak. The further in time one goes, the more likely it is for other events or physical processes to occur that would complicate the spatially-integrated EVE analysis. Duration of dimming may be an interesting parameter to study, but due to the continuing evolution and dynamics of the sun it

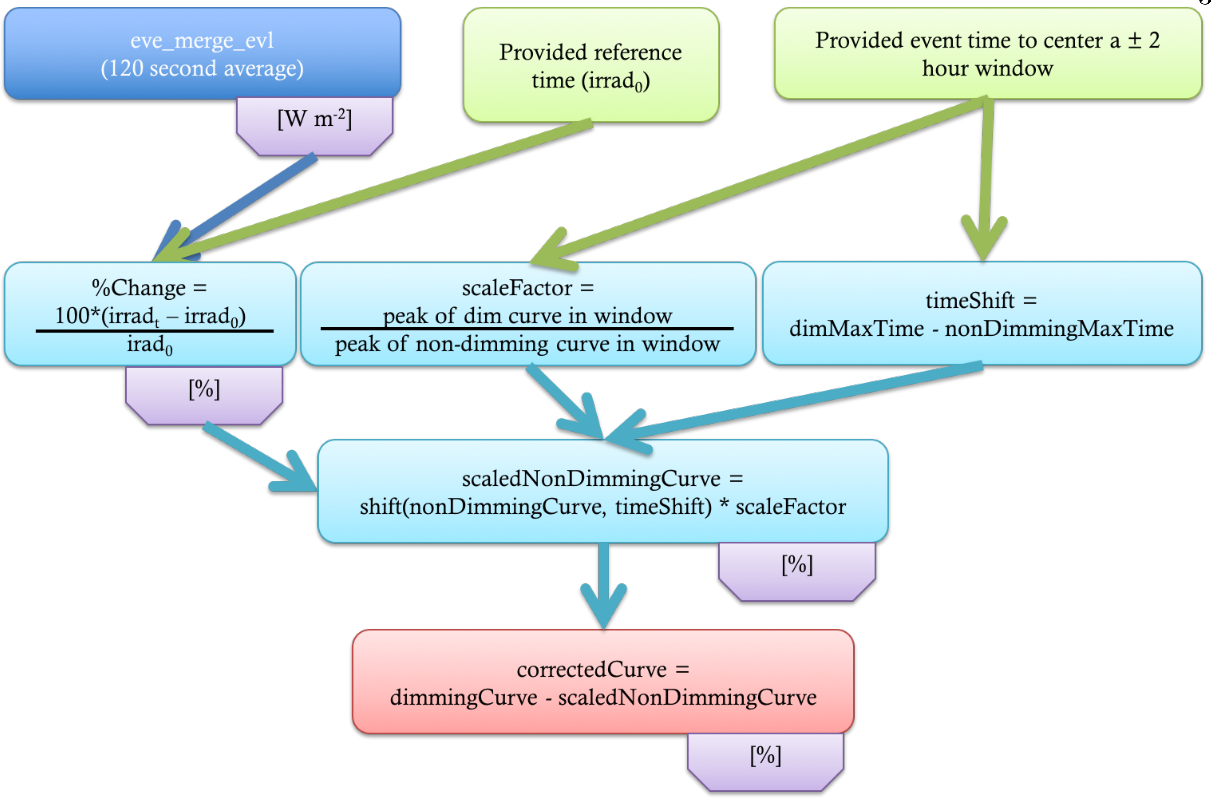

Figure 4.13: Flow-chart for the flare-dimming deconvolution algorithm. Rounded-rectangular boxes describe the steps and the purple boxes indicate the units of the irradiance at that step.

is of secondary priority. Additionally, the duration is likely to be most closely linked to the physical processes responsible for filling plasma back into the void, relaxation of the disturbed system, and temperature evolution causing changes to ionization fractions. All of these have a tenuous connection to CME kinetics and thus provide less promise of providing a physical justification for dimming proxies for CMEs.

Which combinations of dimming and non-dimming line make for the best dimming-isolated light curve? In the simple 2010 August 7 event, it was Fe IX 171 Å (dimming) and Fe XV 284 Å, respectively. In the 28 other cases studied (see Chapter 5), this same combination proved best.

4.3 Error Propagation

Coronal dimming is a transient event lasting several hours that is studied in terms of relative change from the initiation time. As such, no long-term degradation of EVE needs to be factored into uncertainties i.e. the absolute accuracy is not important but the measurement precision is. To estimate precision, a period of solar inactivity was analyzed: 2013 January 28 from 00:00 - 01:00 UT. The estimated precision of these 120-second averaged EVE line data was calculated as the variance of the mean (Bevington, 2003), i.e., the standard deviation divided by the square root of the number of samples, which was 12 in this analysis. Table 4.2 provides the estimated precision for each emission line used in this study, and provides a sense of how well we can detect EVE dimmings that typically have depths less than 5% of the pre-flight irradiance level.

Table 4.2: Estimated precision for selected emission lines in EVE spectra. The Fe IX 171 Å and Fe XV 284 Å emission lines are the choice lines for dimming analysis.

Ion	Wavelength (Å)	Estimated Precision (%)
Fe IX	171	0.06
Fe X	177	0.05
Fe XI	180	0.04
Fe XII	195	0.04
Fe XIII	202	0.04
Fe XIV	211	0.07
Fe XV	284	0.08
Fe XVI	335	0.17
Fe XVIII	94	0.08
Fe XX	132	0.20

These base uncertainties were propagated through each step of the EVE dimming correction method described in Section 4.2. First, the line precisions are combined with the provided reference time to compute percent change (see Figure 4.13, Equation 4.1).

$$\%change = 100 \times \frac{(irrad_t - irrad_0)}{irrad_0} \tag{4.1}$$

where $irrad_t$ is the irradiance at each time and $irrad_0$ is the irradiance at the provided reference time. In practice, the latter is a manually selected pre-flare point that appears to correspond well to a quiet or well-behaved period. All of the uncertainty derivations to follow are based on the basic uncertainty propagation equation,

$$F = f(X, Y) \tag{4.2}$$

$$\sigma_F^2 = \sigma_x^2 (\frac{\partial F}{\partial X})^2 + \sigma_Y^2 (\frac{\partial F}{\partial Y})^2 \tag{4.3}$$

where F is a generic function that will be specified for each of the steps of the deconvolution method. The first step of computing percent change (i.e. where F = Equation 4.1) has the corresponding uncertainty derivation:

$$\frac{\partial F}{\partial X} = \frac{100}{irrad_0} \implies (\frac{\partial F}{\partial X})^2 = (\frac{100}{irrad_0})^2$$

$$\frac{\partial F}{\partial Y} = -\frac{100 \times irrad_t}{irrad_0^2} \implies (\frac{\partial F}{\partial Y})^2 = (-\frac{100 \times irrad_t}{irrad_0^2})^2$$

$$\therefore \sigma_F^2 = \sigma_x^2 (\frac{100}{irrad_0})^2 + \sigma_y^2 (-\frac{100 \times irrad_t}{irrad_0^2})^2$$

$$\implies \sigma_F = \sqrt{\sigma_x^2 (\frac{100}{irrad_0})^2 + \sigma_y^2 (-\frac{100 \times irrad_t}{irrad_0^2})^2} \tag{4.4}$$

where σ_x is the precision of $irrad_t$ and σ_y is the precision of $irrad_0$, which will be identical in this case since Equation 4.1 refers to a single emission line. This is the uncertainty corresponding to $dimmingCurve$ and $NonDimmingCurve$. The next step in the algorithm (see Figure 4.13) is to scale the $NonDimmingCurve$ irradiance so that the peaks of the dimming and non-dimming line have the same magnitude (both of which are now in % units). The derivation for the corresponding uncertainty is,

$$F = xy$$
$$\frac{\partial F}{\partial x} = y, \frac{\partial F}{\partial y} = x$$

$$\therefore \sigma_F^2 = \sigma_x^2 y^2 + \sigma_y^2 x^2 = \sigma_{scaledNonDimmingCurve}^2 \tag{4.5}$$

where x is the non-dimming light curve, σ_x is the result of Equation 4.4 (i.e. the σ_F in Equation 4.4), y is the scale factor (which is a single value), and σ_y is derived as follows:

$$\text{Let} \frac{d}{b} = \frac{dimCurve_{peak}}{nondimCurve_{peak}} = y$$
$$\sigma_y^2 = \sigma_d^2 (\frac{1}{b})^2 + \sigma_b^2 (-\frac{d}{b^2})^2$$
$$\therefore \sigma_y^2 = (\frac{\sigma_d}{b})^2 + (\frac{\sigma_b d}{b^2})^2$$

Thus we have the *scaledNonDimmingCurve* and its associated propagated uncertainty. The final step is to apply the correction to the *dimmingCurve*, which is just a simple subtraction, resulting in the final uncertainty:

$$\sigma_{correctedCurve} = \sqrt{\sigma_{dimmingCurve}^2 + \sigma_{scaledNonDimmingCurve}^2} \tag{4.6}$$

where $\sigma_{dimmingCurve}^2$ comes from Equation 4.4 and $\sigma_{scaledNonDimmingCurve}^2$ comes from Equation 4.5. Evaluation of Equation 4.6 with EVE data results in an uncertainty of $\pm 0.175\%$[4] . Chapter 5 will discuss the passing of the above uncertainty into IDL's *poly_fit* function and the final resultant errors associated with that process.

[4] % here is the same unit as the irradiance, not a percentage of the irradiance value

4.4 Dimming Parameterization Results

4.4.1 Simple Dimming Case

Parameterization of dimming is focused primarily on slope and depth, both of which are selected by eye. The time to select for these parameters is debatable but in this case, we chose depth to be a point soon after the dimming "floor" is reached in AIA Region 1 (red contour and line). Slope was taken to this point, starting from 17:50 UT – the time just before GOES 1-8 Å and EVE 131 Å began to rise. The deconvolution method (Section 4.2) significantly reduces the impact of the flares gradual phase peak to dimming measurements for EVE. Prior to the correction, EVE would have measured a dimming depth of 1.27% in 171 Å and 0.18% in 195 Å. After the correction, these values are 2.94% and 2.09%, respectively. Similarly, slope was changed from 1 % hr^{-1} (171 Å) and 0% hr^{-1} (195 A) to 2.29% hr^{-1} (171 Å corrected) and 2.09% hr^{-1} (195 Å corrected). Furthermore, if this event was being observed in real time, the gradual phase peak makes it impossible to estimate the amount and speed (slope) of dimming accurately. This correction method allows the irradiance increase due to the gradual phase contribution to be compensated in the EVE time series that have dimming.

The small difference in time between different emission peaks – Fe XX peaks 21 minutes before Fe IX in this case – is information that can be used to understand the temperature evolution during dimming. In this event, that time difference is significantly shorter than the hours-long duration of the total dimming event. Thus, it is unlikely that thermal dimming is a significant contributor to the total observed dimming. Instead, our correction method uses nondimming lines as independent measurements of the flare gradual phase profile. Since no dimming is observed in the nondimming lines, the gradual phase profile is assumed to be pure and can then be used as a proxy to remove only the effect of the gradual phase in the dimming light curve with a minimal impact on total dimming. In this way, we can effectively match AIA dimming observations, which are capable of isolating the flaring coronal loops.

The expectation is that the EVE-corrected dimming results should have the same amount of

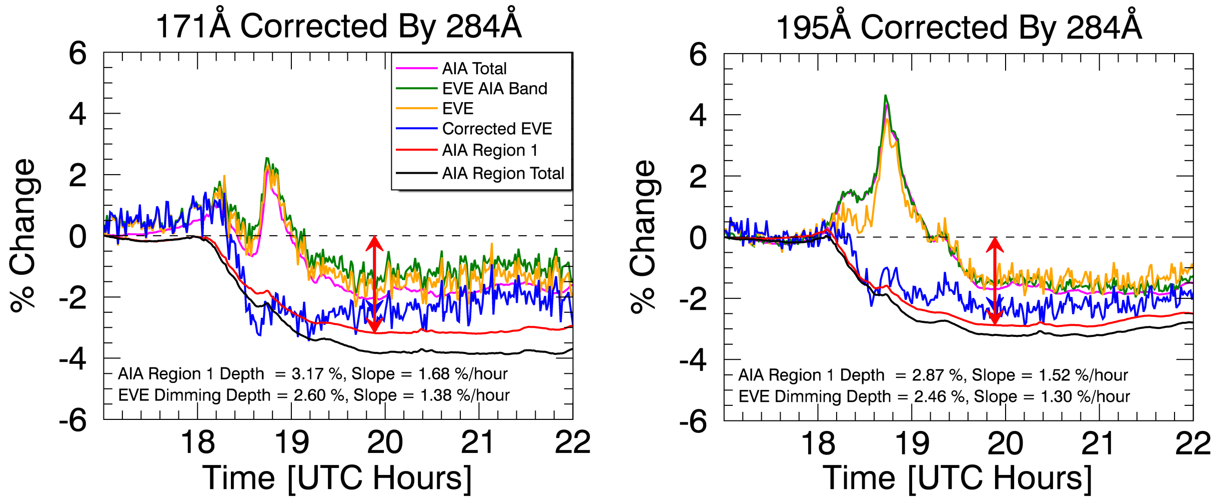

Figure 4.14: Both plots are similar to Figure 4.12 but provide more detail. The left shows results from 171 Å and the right is for 193 Å (AIA) / 195 Å (EVE). The red vertical arrow indicates the point where depth is computed and overlaps a blue vertical arrow indicating the end time of slope computation. The slope range begins at 17:50 UT.

dimming as the AIA results and are also independent of Fe ionization level (in the dimming lines). Figure 4.14 shows the comparison of EVE-corrected dimming time series to AIA results in both 171 Å and 193/195 Å, and Table 4.3 lists the dimming results.

Table 4.3: Key dimming results for 2010 August 7 event. Note that 195 Å in EVE corresponds to the 193 Å band in AIA, which encompasses 195 Å.

Dim line (Å)	AIA Total Depth (%)	AIA Reg. 1 Depth (%)	EVE Depth Corrected (%)	EVE Depth Uncorrected (%)	AIA Total Slope ($\% \, hr^{-1}$)	AIA Rg. 1 slope ($\% \, hr^{-1}$)	EVE Slope Corrected ($\% \, hr^{-1}$)	EVE Slope Uncorrected ($\% \, hr^{-1}$)
171	2.03	3.17	2.60	1.63	1.07	1.68	1.38	0.86
177	–	–	2.79	1.89	–	–	1.48	1.00
180	–	–	2.87	1.98	–	–	1.52	1.05
195	1.68	2.87	2.46	1.52	0.89	1.52	1.30	0.81
202	–	–	2.31	1.60	–	–	1.22	0.85
211	0.52	2.03	2.57	1.60	0.28	1.50	1.36	0.85

AIA Region 1 is considered the reference for mass-loss dimming, so its dimming depth and slope are compared as an estimate of uncertainty for these results from EVE. The differences for the AIA 171 Å and 195 Å dimming depth and slope are 0.3% and 0.16% hr^{-1}, respectively. The relative uncertainty of these is 10% of the mean depth and slope values, being 3.02% and 1.60% hr^{-1}. These differences in the two different AIA bands could reflect the uncertainty that Region 1 is only due to mass-loss dimming and our ability to identify the best Region 1 boundary to encompass the mass-loss dimming phenomena. However, selecting a slightly different boundary did not greatly impact the resultant light curves, so the difference may be real. This would indicate that AIA too sees shallower dimming for higher ionization states if the deconvolution method described in Section 4.2 is not applied. The corrected EVE results for dimming depth and slope have mean values of 2.53% and 1.34% hr^{-1}, and both are 14% less than the AIA Region 1 mean values. The standard deviations for the six EVE lines corrected dimming depth and slope are 0.21% and 0.11% hr^{-1}, respectively. As expected (intended), the EVE corrected results are much more self-consistent with each other than the uncorrected results. The slope tracks the depth variation well; that is, the slope is less when the depth is less. Our expectation was that the slope could represent the CME velocity, and the depth could represent the CME mass loss.

4.4.2 Complex Dimming Case

The dimming parameterization method in this case was the same as in the simple dimming case above. Figure 4.15 shows the analogous plots for this event. While the general trend of EVE follows AIA, it's clear from these plots that applying the same deconvolution methods does not result in as good a match of EVE to AIA. Note that even uncorrected EVE reaches a deeper minimum than the AIA light curves[5] . The only way for the deconvolution method to raise EVE irradiance would be for the nondimming line to have dimming, which would violate the definition. Since this was not the case, all of the corrected/deconvolved EVE light curves (blue) are even lower than the uncorrected EVE dimming line (gold), bringing it further from the AIA "core dimming" light curve (red). Nevertheless, the deconvolution method did successfully remove the flare peak in dimming

[5] Remember that the black line is the total inside contoured areas in AIA, not the total disk

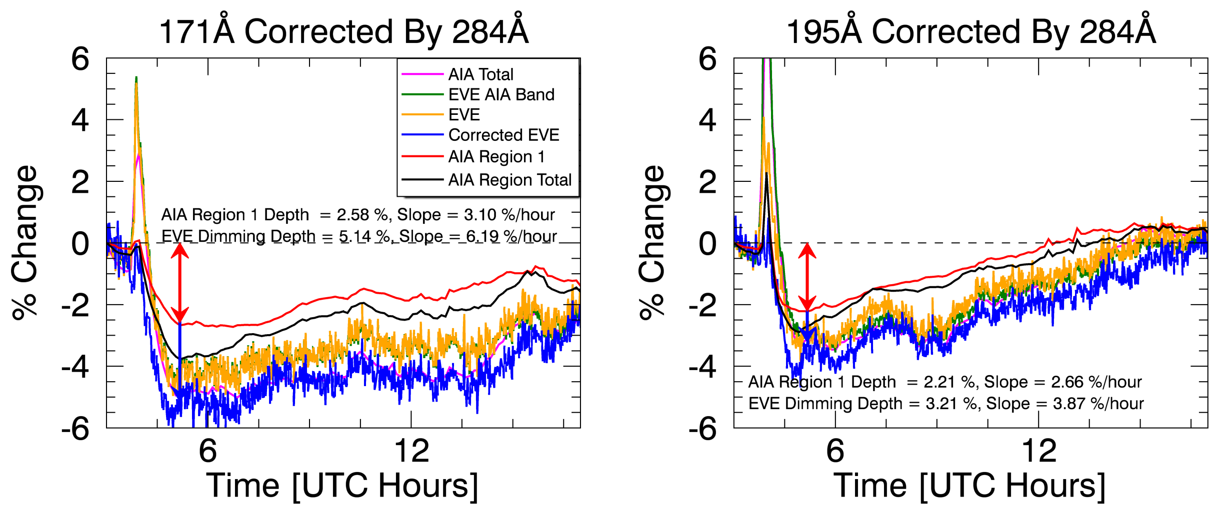

Figure 4.15: Same as Figure 4.14 but for the 2011 August 4, more complex, case. The AIA regions correspond to those selected in Figure 4.9.

lines as can be seen in the difference between the raw EVE (gold) and corrected EVE (blue) light curves. AIA showed that the remaining area (i.e. quiet Sun) had non-negligible dimming (black curve in Figure 4.8 and blue in Figure 4.9). Adding that to the AIA total dimming for 171 Å would result in a peak dimming of about 4% – still 1% lower than what is seen in EVE. Doing the same for 195 Å would get the two to match within 1%. The analysis is further complicated by the fact that the AIA bandpasses are several nanometers wide causing blending of many emission lines and continuum that makes direct comparison with EVE difficult, particularly for an event with so many simultaneous physical processes involved, each of which has an impact on the irradiance that can vary through time.

The ultimate goal of the dimming analysis is to provide proxies for CME mass and velocity. This event was included in the semi-statistical study to determine the relationship between those CME parameters and the dimming depth and slope that will be discussed in Chapter 5.

4.5 Case Studies Summary

To summarize the physical processes taking place in the simpler 2010 August 7 event, the plasma and its irradiance have source and sink terms. Near the beginning of the flare, heating is very dominant and causes a rapid increase in high ionization states for the various Fe emissions. Later in the flare, cooling of the plasma causes an increase in lower ionization states, and those cooler lines peak later than the hot lines. Through it all, the mass ejection can act as a sink for most coronal emissions. Early in the flare, before the low ionization states have been strongly affected by the cooling described above, the mass ejection dominates and causes the irradiance to visibly drop. Much later in the flare process, as the plasma approaches its preflare level, the missing plasma again becomes apparent in the irradiance time series as an hours-long, few-percent decrease. Quantitative dimming results are summarized in Table 4.3.

The physical interpretation of the more complex 2011 August 4 event is more difficult to obtain. The size of the flare was nearly an order of magnitude larger than in the simpler 2010 August 7 case and the associated CME velocity was 1.5x faster – together, these are a general indicator that the amount of energy involved in the eruptive event was much larger in the more complex event. Additionally, the pre-eruption state of the Sun was more complex for the 2011 August 4 event, as evidenced by the more numerous active regions and polar filament, the coronal streamers, and the proximity of active regions to the one responsible for the eruption itself. All of this means that more energy was released via more mechanisms. The EUV wave was much more prominent in this case, sympathetic responses were clear, and heating (rather than cooling) dominated the irradiance indicative of energetic processes dominating relaxing ones. Quantitative dimming results are summarized in Table 4.1.

Chapter 5

Semi-Statistical Study of Dimming-CME Relationship

Extreme ultraviolet (EUV) coronal dimmings are often observed in response to solar eruptive events. These phenomena can be generated via several different physical processes (see Chapter 3). For space weather, the most important of these is the temporary void left behind by a coronal mass ejection (CME). Massive, fast CMEs tend to leave behind a darker void that also usually corresponds to minimum irradiance for the cooler coronal emissions. If the dimming is associated with a solar flare, as is often the case, the flare component of the dimming in the cooler coronal emission can be isolated and removed from the dimming light curve using simultaneous measurements of warmer coronal lines (see Chapter 4). In the present Chapter, we apply this technique to 38 dimming events: the two case studies from Chapter 4 plus 36 additional events taken from two separate two-week periods in 2011. Dimming is then parameterized in terms of depth and slope for each of the events. We provide statistics on which combination of wavelengths worked best for the correction method, describe the fitting methods applied to the dimming light curves, and compare the dimming parameters with corresponding CME parameters of mass and speed. The best linear relationships found with an accuracy of about 20% are that the CME speed is about $630 km\ s^{-1}$ times the dimming slope ($\%\ hour^{-1}$) and the CME mass is about $1.03 \times 10^{15}\ g$ times the dimming depth (%). These relationships could be used for space weather operations of estimating CME mass and speed using near-realtime irradiance dimming measurements.

5.1 Introduction to Dimming and CME Parameterization and Statistics

Extensive surveys of coronal dimming events and their relation to CMEs have been performed by Reinard and Biesecker (2008, 2009). For their sample of 100 dimming events, Reinard and Biesecker (2008) found mean lifetimes of 8 hours, with most disappearing within a day. Reinard and Biesecker (2009) studied CMEs with and without associated dimmings, finding that those with dimmings tended to be faster and more energetic. Bewsher et al. (2008) found a 55% association rate of dimming events with CMEs, and conversely that 84% of CME events exhibited dimming. The timescale for dimming development is typically several minutes to an hour. This is much faster than the radiative cooling time, which implies that the cause of the decreased emission is more dependent on density decrease than temperature change (Hudson et al., 1996). Dimming regions occur on a spatial scale similar to CMEs, more so than other CME-associated activity (such as flares and EUV waves). Studies have demonstrated that dimming regions can be a good indicator of the apparent base of the white light CME (Thompson et al., 2000; Harrison et al., 2003; Zhukov and Auchère, 2004). Thus, dimmings are usually interpreted as mass depletions due to the loss or rapid expansion of the overlying corona (Hudson et al., 1998; Harrison and Lyons, 2000; Zhukov and Auchère, 2004). Spectroscopic observations of coronal dimmings (Harra and Sterling, 2001; Harrison et al., 2003; **?**) found blueshifts in several coronal lines, indicating outflow in dimming regions. Dimmings have also been shown to extend deep into the corona and possibly the chromosphere and photosphere (**?**). When dimmings are present with a CME, they are one of the earliest signatures of the actual mass ejected from the low corona, and provide unique information on the onset time and location of the ejection. Many landmark studies have established that dimmings can contribute a large fraction of the mass to a CME (Harrison and Lyons, 2000; Harrison et al., 2003; Zhukov and Auchère, 2004; Aschwanden et al., 2009a). There are well-established methods to derive the mass properties of CMEs, but there are still outstanding questions involving the source of the CME mass: how much of the mass comes directly from the erupting region, how much comes from the surrounding or overlying large-scale corona, and how much is ”swept up” as the CME propagates (Bein et al., 2013).

An Earth-directed CMEs potential geoeffectiveness is typically characterized by three values: its velocity, mass, and the magnitude and duration of the southward component of the magnetic field (B_z) impacting Earth. Typical CME forecasts provide a predicted Earth arrival time only. The geomagnetic storm magnitude is strongly linked to the CME momentum and magnetic field orientation while arrival time at Earth is primarily dependent on CME velocity. The current standard process for estimating velocity relies on sequential coronagraph images from SOHO/LASCO and STEREO/SECCHI. There are ground-based white light coronagraph measurements, such as by High Altitude Observatorys K-Cor instrument, but those measurements are limited to the low corona and constrained by the times that the sun is at a sufficiently high elevation as viewed from a fixed-position on Earths surface (typically <6 hours/day). Analysis of coronagraph images to determine CME velocities and masses results in relatively large uncertainties of 30-50% (**?**Vourlidas et al., 2010; **?**). The velocity and mass measurements with the most uncertainty are for Earth-directed CMEs that are seen as halos in coronagraphs at or near Earth. For these CMEs, a velocity is significantly affected by projection on the plane-of-sky, and a large percentage of the mass can be hidden behind the instruments occulter. Without observations of these CMEs from another viewpoint, such as STEREO, it is difficult to make an accurate measurement of the CME velocity and mass from the coronagraph observations. However, dimmings associated with these CMEs are very well observed by Earth-based observations. Our studies of coronal dimming events have focused on the possibility of coronal dimming observations providing useful indicators for CME velocity and mass, and can readily be combined with most B_z prediction methods.

While earlier studies showed that dimmings can account for a significant fraction of the mass ejected, multi-viewpoint observations using STEREO data have the advantage of providing independent mass measurements for the same event from two different aspect angles, yielding a better mass accuracy. In a survey of six STEREO events observed as dimming by EUVI and as CMEs by COR2, Aschwanden et al. (2009a) found a clear correspondence between the EUV and white light mass estimates. Colaninno and Vourlidas (2009) developed a triangulation method to estimate the true (accurate) mass of CMEs from SECCHI observations. More recently, Bein et al. (2013) applied similar methods to a larger CME sample (25 events) and over an extended height range, allowing them to remove the effects of the CME emerging from behind the occulter and to calculate the mass flux of the CMEs in the lower corona.

Standard plane-of-sky velocity estimates are made and cataloged by the Coordinated Data Analysis Workshops (CDAW) CME catalog (Gopalswamy et al., 2009), which use routinely produced SOHO/LASCO coronagraph images. The different views from LASCO and SECCHI images can be used to better constrain the velocity, direction, and mass of CMEs (e.g., Colaninno and Vourlidas 2009). None of these methods can be used to estimate B_z but velocity is of particular use to space weather forecasters for predicting Earth-arrival times.

In the present chapter, we analyze 38 coronal dimming events – the two from Chapter 4 plus 36 more during two separate two-week periods during 2011 – and search for the relationship between dimming and CME velocity and mass. Of the events studied, 17 could be parameterized in both dimming with EVE data and CME velocity from LASCO and SECCHI observations, and 14 events in dimming with EVE data and CME mass from the coronagraph observations.

Section 5.2 shows some examples of observations and describes the method for selecting this sample of events and explains why some events identified in AIA could not be analyzed with EVE and/or SECCHI. Section 5.3 provides examples and statistics on the flare-peak correction method detailed in Section 4.2, specifically which combinations of dimming and non-dimming lines provided the best correction for each of the events. Section 5.4 describes the fitting method applied to the deconvolved EVE light curves, including a discussion of uncertainties. Section 5.5 discusses the parameterization of fitted dimming light curves and CMEs observed in coronagraphs. Finally, Section 5.6 shows the correlations between the various combinations of coronal dimming and CME parameters, and conclusions about dimming and CME relationships are presented in Section 5.7.

5.2 Observations and Event Selection

In addition to the two cases studied in detail (see Chapter 4), four weeks were selected in 2011 for analysis of coronal dimming events: February 10-24 and August 1-14 (Figure 5.1). These two independent periods about 6 months apart were chosen as appropriate times during the initial rise of solar activity during solar cycle 24. The initial criterion for this selection is to have a total period of time that could result in more than 30 identifiable events. It is also desirable to select a time when the two STEREO spacecraft orbital locations were advantageous for geometric analysis, and when the other space-based instruments used in this study could be expected to be operating nominally. The periods of study are typical in terms of CME occurrence and solar EUV irradiance variability, both near their mean values (see Figure 5.1).

Images from AIA were used to first identify dimming events. Identification was performed manually using daily AIA movies to create a list of candidate events. Two people made the identifications separately, looking at different movies. James Mason used the AIA 211-193-171 Å composite movies (e.g., Figure 4.4) and Dave Webb used the 193 Å movies. The primary initial selection criteria were that 1) the dimming must persist for several hours and 2) the dimming have non-trivial spatial extent e.g., at least comparable to the size of an active region. The independently identified events were then accumulated, duplicates merged as positively identified events, and disparities investigated by each identifier. Sometimes disparities proved to be questionable events according to the selection criteria above and were removed from the event list. Other times the disparities proved that the independent analysis acted as a failsafe – a single observer simply missed an event but the other caught it. Future studies will use the automated AIA dimming detection method developed by Krista and Reinard (2013).

Once the event list was deconflicted, the approximate time of the event was used to search the related observations in other instruments: flares from GOES X-ray flux, CMEs from LASCO and COR, and solar irradiance from EVE. This initial list included 38 events (includingw the 2010 August 7 simple case from Chapter 4, which was outside the four week period). In some

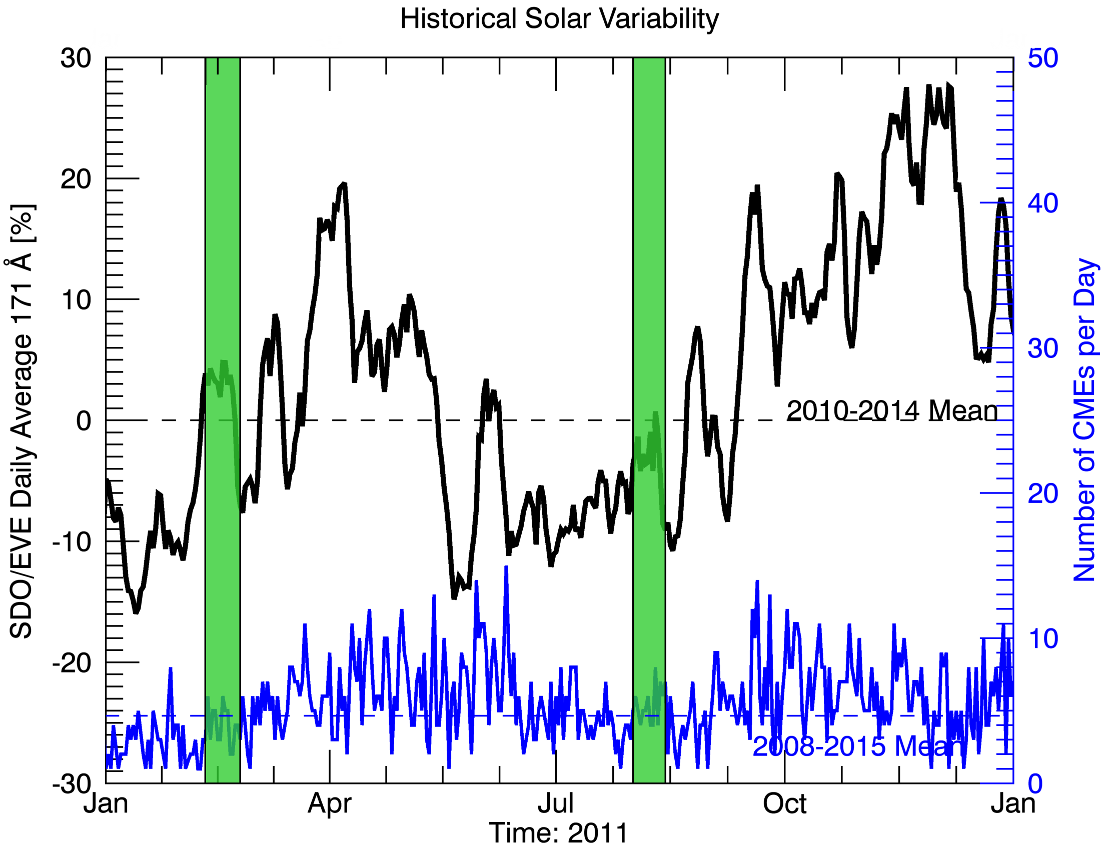

Figure 5.1: Context for the selected periods of study. The black line is the daily averaged EVE Fe IX 171 Å line and the blue line is the daily total CME occurrence. The vertical green bars indicate the selected periods of this study. The mean for EVE (dashed black line) is taken over the first four years of EVE's operations (2010-2014) and the mean for CME occurrence (dashed blue line) is taken for the most recent solar cycle starting in 2008 to the present date.

cases, the dimming was not clear in EVE data or the CME was not clearly identified in the coronagraph images; nevertheless these were dimmings identified in AIA and are listed in Table 5.1 for completeness. Appendix A expands the event list with ancillary data such as dimming and CME parameterization values. 29 of these events could be parameterized with EVE, 21 had measured CME velocities, and 17 had measured CME masses. Six of the CMEs had at least 2 views so that 3-D analysis could be applied for improved accuracy of the CME kinetic parameters.

Table 5.1: Event list. Times and locations are approximate. The derived parameters columns abbreviations are as follows: V = velocity, M = mass, 3V = 3-D velocity, 3M = 3-D mass, D = depth, S = slope. Only 29 of the events have dimming and CME derived parameters to allow the study of the relationships between dimmings and CMEs. See Appendix A for event list with ancillary data.

Event #	Date	Time [UT]	Location	EVE Derived Parameters	CME Derived Parameters
1	2011 Feb 10	07:40	N20 W-limb	D, S	–
2	2011 Feb 10	13:36	N20 W-limb	D, S	V, M
3	2011 Feb 11	07:46	N20 W-limb	D, S	V, M
4	2011 Feb 11	13:21	N60 W00	D, S	–
5	2011 Feb 11	21:43	N10 E-limb	D, S	V, M
6	2011 Feb 12	06:05	N30 E10	D, S	–
7	2011 Feb 13	14:00	S10 E10	D, S	3V, 3M
8	2011 Feb 14	15:45	S10 W00	D, S	V, M
9	2011 Feb 14	17:36	N30 E20	–	3V, 3M
10	2011 Feb 15	02:07	N00 W00	D, S	3V, 3M
11	2011 Feb 16	14:40	S20 W30	D, S	–
12	2011 Feb 17	00:47	E40 W00	D, S	–
13	2011 Feb 18	11:15	S10 W50	D, S	V, M
14	2011 Feb 17	19:20	N30 W00	D, S	–
15	2011 Feb 24	07:40	N10 E-limb	D, S	–
16	2011 Feb 25	07:00	N45 E60	D, S	V, M
17	2011 Aug 2	05:10	N05 W20	D, S	V, M
18	2011 Aug 2	13:00	N00 E-limb	D, S	–
19	2011 Aug 3	13:43	N05 W48	D, S	V, M
20	2011 Aug 4	04:12	N05 W58	D, S	V, M
21	2011 Aug 4	04:41	N80 W00	–	V
22	2011 Aug 5	07:25	S30 E50	–	–
23	2011 Aug 6	11:50	S14 E10	D, S	–
24	2011 Aug 6	18:25	N05 W25	–	–
25	2011 Aug 6	17:35	N30 W-limb	–	V, M
26	2011 Aug 6	22:40	N10 W25	D, S	–
27	2011 Aug 7	04:00	N10 W55	D, S	V, M
28	2011 Aug 8	01:15	N80 E05	–	–
29	2011 Aug 8	11:00	N15 W70	–	–
30	2011 Aug 8	17:42	N05 W05	D, S	–
31	2011 Aug 8	18:42	N05 W75	–	3V, 3M
32	2011 Aug 9	08:10	N15 W70	D, S	3V, 3M
33	2011 Aug 9	09:12	S30 E-limb	–	–
34	2011 Aug 9	11:26	N05 W00	D, S	V, M
35	2011 Aug 11	10:23	N00 W-limb	D, S	3V, 3M
36	2011 Aug 12	00:09	N45 E80	D, S	V, M
37	2011 Aug 12	11:13	N50 E70	D, S	–
38	2010 Aug 7	18:05	N05 E60	D, S	3V, 3M

Because EVE irradiance observations are spatially integrated, dimmings from spatially-distant areas that occur too closely in time overlap in the irradiance time series and cannot be easily separated and parameterized. Thus, such events have a "–" in Table 5.1 and are excluded from the correlative study in Section 5.6. This was the case for Events 9, 21, 29, 31, and 33. Similarly, Event 22 was a series of small eruptions from an active region with multiple slow CMEs whose analysis would be difficult. Secondly, some dimmings identified in AIA were not detectable in the EVE data making parameterization impossible. Here, "not detectable" simply means that the EVE light curves did not show anything resembling the archetypal dimming near the time that was identified in AIA. This implies the magnitude of the dimming was small ($< 1\%$ impact on irradiance), which would be the case if the dimming itself was not very deep or if evolution elsewhere on the solar disk dominated (e.g., active region evolution). Examples of the former are Event 24, which was a very slight darkening of an active regions coronal loops with no identified CME; Event 28, which was a small occurrence of "coronal rain", also with no identified CME; and Event 25, which was an off-disk dimming event with a narrow CME. In principle, it is possible for off-disk events to generate a large irradiance change, but in this case the change was insufficient to be observable by EVE. In total, these criteria on EVE measurements resulted in 9 of the 38 events being excluded from the correlation analysis, leaving 29 events. These 29 can be processed using the flare-dimming deconvolution method described in Section 4.2. The next section will discuss the results of this process.

5.3 Flare-Dimming Deconvolution Method Statistics

There are 30 permutations of the dimming (171, 177, 180, 195, 202, 211 Å) and nondimming (211[1] , 284, 335, 94, 131 Å) lines for the correction method. Each one is processed using the same algorithm described in Section 4.2. Figure 5.2 shows an example of all 30 combinations for a single event (Event 20). It can be seen that the the higher the ionization state of the nondimming line, the "purer" the flare light curve, i.e., higher ionization states return almost perfectly back to

[1] Again, note that 211 Å is included in both dimming and nondimming categories to reflect its ambiguity

their pre-flare irradiance level soon after the peak while lower ones show some additional response. Because the most intense heating occurs early in the flare, during the impulsive phase as observed by e.g., GOES or RHESSI HXRs, it's unlikely that the emission from high ionization states disappears because it was heated to the next ionization state. Rather, it returns to its preflare level because the intense heating supporting its existence is over and cooling has set in. Indeed, the mid-ionization states such as Fe XVI at 335 Å show a slow, hours long, ramp downward in irradiance. The fact that these mid-ionization states don't immediately return back to their preflare level indicates that either the net cooling rate at those temperatures is slower than at higher temperatures and that the cooling is ongoing during this hours-long period. In other words, warm ions like Fe XVI are slowly gaining back electrons and acting as a source to the cooler ionization population like Fe IX. Critically, this "feeding" of the Fe IX population is a cooling mechanism, not a mass-loss one. By removing this trend as indicated by the irradiance in e.g., Fe XV 284 Å, we obtain a light curve more sensitive to mass-loss than temperature evolution (black curve in Figure 5.2).

In Chapter 4, it was found that for the 2010 August 7 event, the combination of Fe IX 171 (dimming) and Fe XV 284 (non-dimming) in EVE gave the best match to the spatially isolated dimming in AIA 171 Å. The only dimming mechanisms identified to be important in this event were mass-loss and thermal. Thus, it seems that the 171 Å - 284 Å combination can successfully mitigate the impact of thermal processes on the dimming line. If other dimming mechanisms play an important role in the irradiance, as is the case for the 2011 August 4 case in Chapter 4, it may be necessary to account for them such as by identifying and removing the impact of obscuration dimming. Until such an analysis is performed, we apply the deconvolution method to the additional 28 events with viable EVE data using the clean removal of the flare peak as the criteria for determining the best combination of dimming-nondimming line. In other words, the peaks of the dimming and scaled/time-shifted nondimming lightcurves should be similar in shape. Figure 5.2 shows that many of combinations would meet this criteria. The next determining factor is depth of dimming. Event 20 had a relatively consistent depth of dimming for all dimming lines, but this is not the case for all events. Generally, we prefer a larger magnitude dimming as its interpretation is less ambiguous and less susceptible to being dominated by other physical processes such as active region evolution. As was shown in Chapter **??**, the ionization level is inversely proportional to depth of dimming. Thus, 171 Å is generally preferred as the dimming line but is evaluated on a case by case basis for the events studied here. Finally, all other things being equal, we prefer to use 284 Å as the nondimming line for deconvolution based on the physical motivation provided in the paragraph above.

This methodology has been applied to the 28 unique EVE dimmings found during the four weeks studied. Of these, all 28 were found to be best represented by the 171 Å - 284 Å combination. It is possible that other coronal line pairings might be better for different spectral resolution measurements. We will gain additional confidence in the effectiveness of this line pairing for EVE if we find a positive and statistically significant correlation between corrected EVE light curve parameterizations to independently derived CME mass and velocity. The first step in that process is to fit the EVE light curves in preparation for dimming parameterization.

5.4 Dimming Light Curve Fitting Method

5.4.1 Physics Motivation and Fit Types

The β parameter for a plasma is an indicator of the relative importance of plasma and magnetic pressures, expressed as

$$\beta = \frac{p_{plasma}}{p_{mag}} = \frac{nk_bT}{B^2/(2\mu_0)}$$

where p is pressure, n is number density, k_b is Boltzmann's constant, T is temperature, B is magnetic field strength, and μ_0 is the permeability of free space. In the solar corona, β is typically ¡ 1, indicating that the magnetic field dominates the flow of plasma, i.e. plasma is confined by magnetic fields. Thus, in the initiation of a CME where magnetic fields are propelled out of the corona and expand as they do so, the plasma in the enclosed bubble of the CME experiences an adiabatic expansion and density decrease (Figure 5.3). Aschwanden et al. (2009b) described this

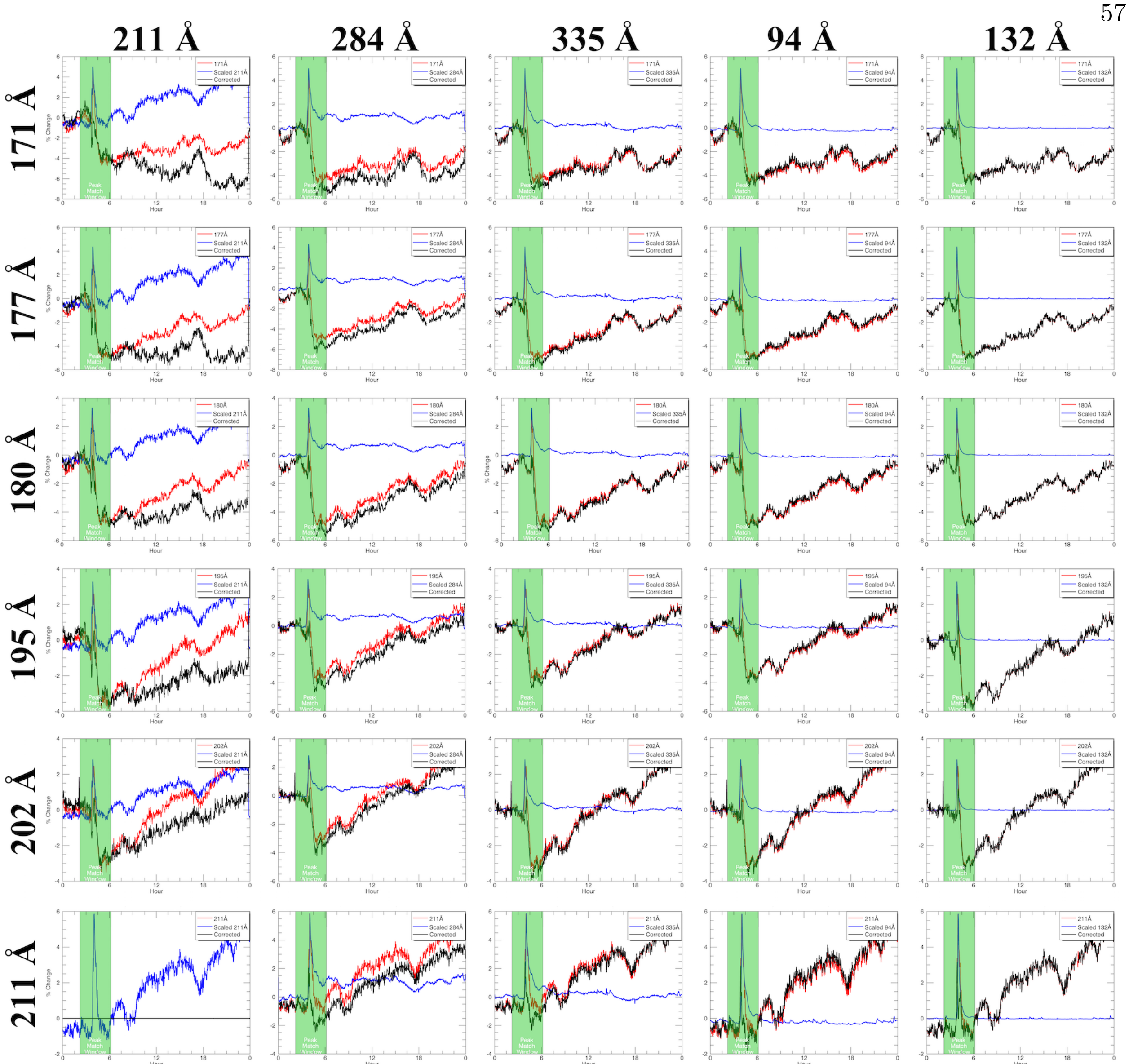

Figure 5.2: Example of every combination of the dimming (rows) and nondimming (columns) lines for the deconvolution method for a single event (Event 20). In each plot, the red is the dimming line, blue is the scaled and time shifted nondimming line, and black is the result of the subtraction (red - blue). The vertical transparent green bar indicates the time window the algorithm uses for finding and matching peaks.

process and here we adapt it for the variation of intensity in collisionally-excited lines as a function of height for a constant-temperature and expanding volume:

$$\frac{I(t)}{I_0} \propto \left(\frac{h_0}{h(t)}\right)^3 \tag{5.1}$$

where $I(t)$ is the bubble intensity as a function of time t, I_0 is the intensity at an initial time, and h is the corresponding height. Note that height as a function of time is a speed. This simple power-law description does not account for any complicating factors such as thermally-induced emission changes, interaction with overlying coronal magnetic fields, or later recovery of the regional emission. Aschwanden (2009) developed a more sophisticated model of dimmings, including adiabatic expansion and gravitational stratification. However, the model contains 14 free parameters and is more suited to a case-by-case study of dimming morphologies. For the purposes of our correlative study, it is reasonable to assume that the decrease in emission due to the volume density is more significant than the thermal and inhomogeneity effects, and that the effective height scale of the CME is the most important parameter.

In Equation 5.1, as time tends to infinity, the local emission goes to zero. However, the solar irradiance, as observed by EVE, decreases to a constant background value during a dimming event. Thus, this simple power-law fit for the EVE dimming events can not be used directly. Furthermore, the relationship of height and time is not well established, so different functions are fitted to the EVE dimming events to explore which functions are more optimal for determining the dimming event parameters of depth and slope.

Exponential and power law fits tend to result in $\chi^2 > 20$, meaning they were very poor fits. Polynomial fits up to order five were also computed, with 5th and 3rd orders appearing to best describe the shape of the light curves (see Figures 5.4 and 5.5). Although the 3rd order polynomial function is expected to be a better match to the theory, the best-fit function is used for deriving the dimming slope and depth.

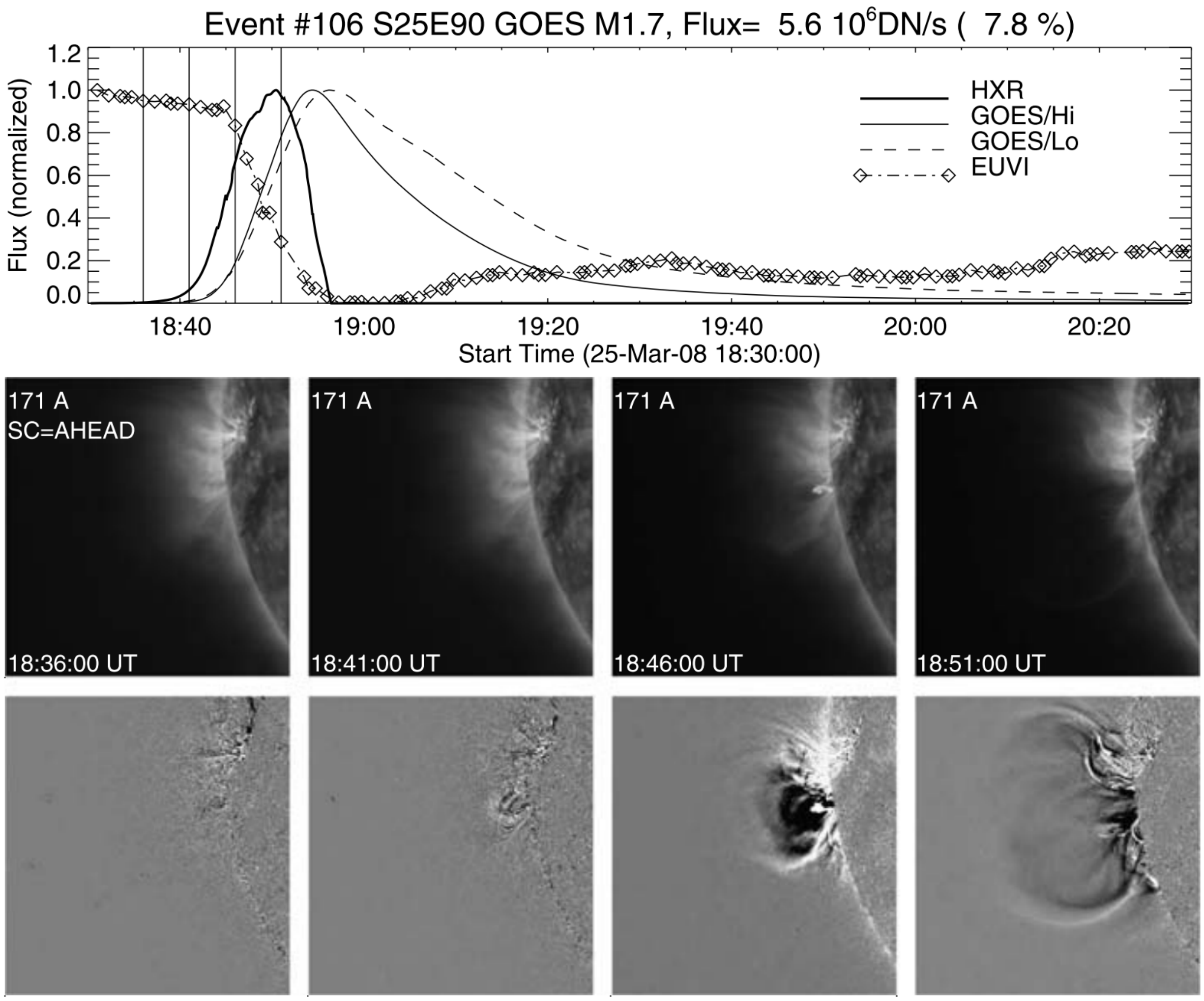

Figure 5.3: Example of CME bubble expansion and associated EUV dimming. (Top) Soft X-ray (GOES/Lo 0.5 4 and 1 8 , thin curves) and EUV (STEREO-A/EUVI, diamonds) light curves and time derivative, dI(t)/dt, of the harder soft X-ray light curve (thick solid line) for the flare/CME event on 2008 March 25 at 18:30 UT. (Bottom) Four STEREO-A/EUVI images (top row) and running-difference images (bottom row). Note the strong dimming in the EUV light curve. The diamond symbols mark the times of the EUV images; the selected images shown below are marked with vertical lines. The peak EUV flux is $F = 5.6 \times 10^6 DNs^1$ (or 7.8% of the total flux). The field of view of the images is 512 EUVI pixels (600 Mm). Adapted from Aschwanden et al. (2009b).

5.4.2 Dimming Fit Uncertainty Computation

The uncertainties from Section 4.3 correspond to the deconvolved/corrected EVE dimming light curve. Those light curves are the input for the fitting function, IDL's *poly_fit*, which also

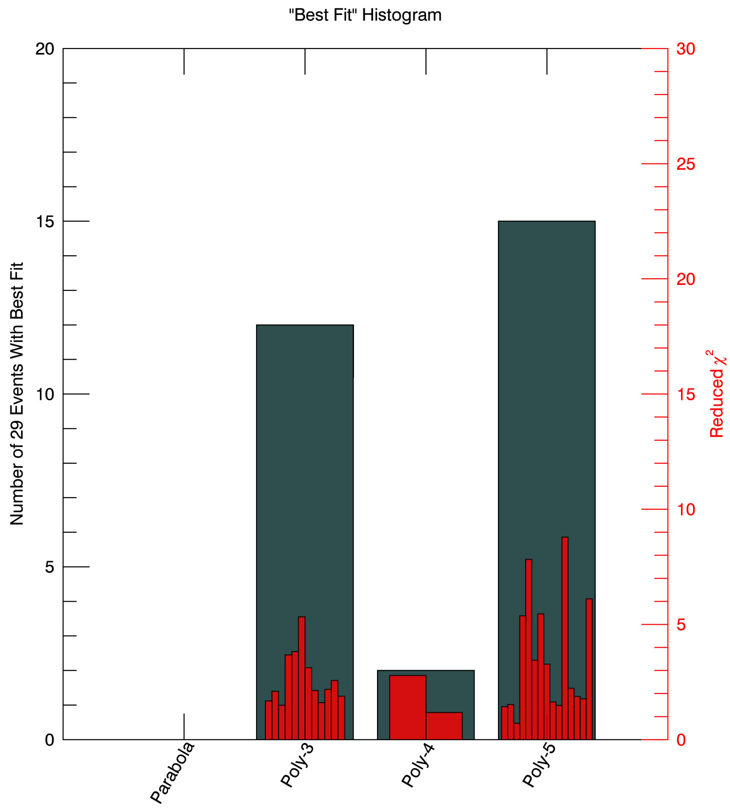

Figure 5.4: (blue) Statistics of manually selected "best fit for all unique EVE dimming events in 4 weeks studied and (red) the reduced χ^2 for the best fits. The 3rd and 5th order polynomial fits provided the largest number of best fits.

accepts an input *measure_errors* for uncertainties. Figure 5.5 shows polynomial fits from 2 to 5 with the measurement errors and the resultant 1σ uncertainties computed by *poly_fit*. The fits achieve the desired effect of reducing uncertainty even further and providing a smooth function to parameterize.

5.5 Parameterization Methods

Dimming and CMEs are complex phenomena with complex observations and associated data analysis. Our end goal is to provide simple measures of dimming to act as proxies for CME mass and speed, driven by a physical explanation. Given this, the space weather community would

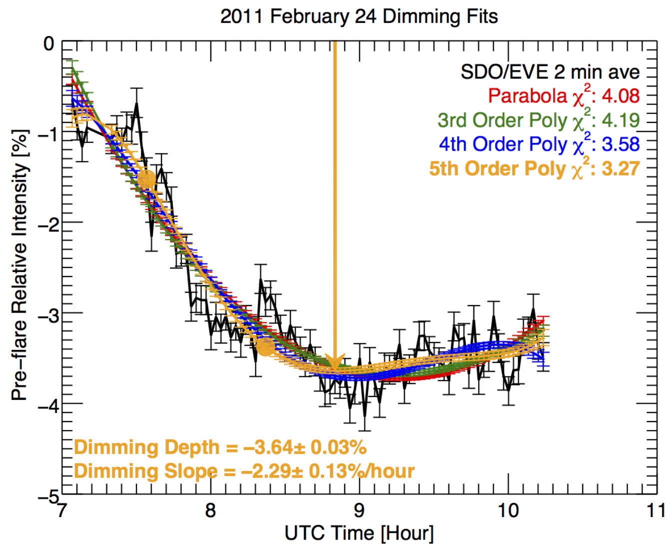

Figure 5.5: A single dimming event (Event 15) showing the reduction in uncertainties of the fits compared to the EVE data. The arrow shows the location of dimming depth parameterization for this event, and the two filled circles indicate the range where slope was computed. Their colors correspond to the fit types in the legend. The lowest indicates that the 5th order polynomial was the best fit for this event, but we note that the results from the other polynomial fits are very similar.

have an independent indicator of CME presence and importance to geospace, and the astronomy community would have a means of detecting and characterizing CMEs on other stars (albeit a first-order characterization). To that end, this section describes the parameter derivations for dimming and CMEs that will be used to establish a correlation in Section 5.6, motivated by the physics in preceding sections.

5.5.1 Dimming Parameterization

Points for the computation of slope and depth are selected manually from the best fit light curve from Section 5.4. Slope point selection was guided by the desire to have χ^2 near unity and by some flexibility for events where the EVE dimming correction method did not completely remove the flare peak of the cool corona line (Fe IX 171 Å). In such cases with a residual flare peak, the fits can deviate from the "pure" dimming light curve and skew the upward. Rather than develop a complicated algorithm to account for this effect autonomously, selection of the best fit was done by manual inspection. Dimming slope was computed across a range: the initial point was typically chosen to be soon after the initial dimming rollover when the slope becomes relatively constant, and the final point was selected just prior to the inverse rollover leading to the relatively flat period in the light curve (see solid circles Figure 5.5). The slope need not be constant between these two points. For each time step within the selected range, the derivative was computed. The single-value slope parameter for each event is the mean of these derivative (slope) values. The dimming depth parameter is taken from a relatively stable pre-flare value to a point near the beginning of the dimming floor (see arrow in Figure 5.5).

The uncertainty associated with dimming depth is just the uncertainty of the fitted light curve at the point selected for the depth measure, as exemplified by the error bar at the arrow in Figure 5.5. The uncertainty for slope requires some additional computation. To compute the derivative of the light curve at each point within the specified time range, IDL's *deriv* function is used; the corresponding *derivsig* function returns the 1σ uncertainty for each point in the derivative array. Collapsing the various derivatives into a single slope parameter via the mean has the corresponding uncertainty,

$$\sigma_{slope} = \frac{1}{N}\sqrt{\sigma_1^2 + \sigma_2^2 + ...\sigma_n^2}$$

where N is the number of points, and $\sigma_1 ... \sigma_n$ are the uncertainties for each point returned from *derivsig*. Appendix A includes the dimming depth, slope, depth uncertainty, and slope uncertainty for each of the 38 events studied.

5.5.2 CME Parameterization

The detailed 3-D analysis of the velocity and mass was possible for six of the best-observed CMEs, using either or both LASCO and the CORs data. These six events are noted as 3V, 3M in Table 5.1 and shown as solid red symbols in Figure 5.6. Following the method of Colaninno and Vourlidas (2009), the GCS model is fit to the observations to determine the 3-D location and heights of the CMEs. The 3-D heights and longitude of the CME are needed to calculate the "true" 3-D mass of the CME. These heights are also used to calculate the de-projected velocity of the CME. The reported masses are for a height of 15 R⊙, using the fitting method of Bein et al. (2013) for mass increase with height. For the 2011 February 13-15 CMEs the mass was measured in both COR2A and COR2B and then averaged. For the 2011 August 9 and 11 CMEs, the mass was measured in LASCO-C3 only.

The following procedure was used to estimate the uncertainties for the CME kinetic parameters. The LASCO CDAW measurements were used for most of the events to derive the CME velocity and mass, which are based on a single viewpoint observation as opposed to 3-D. The reported linear speed of each CME is obtained by fitting a straight line fit to the height-time measurements at a fixed position angle. If we assume conservatively that the CME axis is 60°from the sky plane as the worst case (for non-halo CMEs), this results in a factor of 2 (50%) underestimation of the speed. The CDAW catalog also provides the CME span angle, which can be used to provide an estimated error on the CME mass (Figure 4 of Vourlidas et al. 2010). As an example, if we take Event 2 from Table 5.1 above, then using these errors we have $speed = 338 \pm 345 km\ s^{-1}$ and $mass = 3.40 \times 10^{14} \pm 4.30 \times 10^{14}\ g$.

For the six events with 3-D analysis of the CME measurements, we derive the error in the speed from the linear fit to the data assuming the error in the 3-D height measurements is $\pm 0.48 R\odot$ (Colaninno et al., 2013). Thus, if we take Event 7 as a typical 3-D CME measurement, we get $353 \pm 13\ km\ s^{-1}$ for the speed. The mass is still considered an underestimate from the 3-D analysis but is better determined because the plane-of-sky angle and 3-D heights are known from the GCS model fit, so a ±15% error is assumed for the 3-D mass estimates (Bein et al., 2013).

For the purpose of linear-fitting with dimming parameters in Section 5.6, the midpoint between the low and high limits is chosen for each CME speed and mass parameter reported here, and the CME parameter error is the range between the high and low limits divided by two (i.e., ± error bars in Figure 5.6). The plot of the points themselves does not display this center-point for single-viewpoint derived CME parameters but does for 3-D derived CME parameters. Appendix A includes the CME speed, mass, speed uncertainty, and mass uncertainty for each of the 38 events studied.

5.6 Dimming and CME Parameters Correlation

As described in Chapter 4, we expect direct proportionality between dimming depth and CME mass, and between dimming slope and CME velocity. In other words, there should be a stronger correlation between these parameters than between any other combination of parameters. The analysis of just two events in that chapter does not establish any such possible relationships. This study is a more in-depth examination of such possible relationships with many more events. While our intention for this study was to have 30 events, it was challenging to obtain CME velocity and mass for all of the candidate events. Nevertheless, there was a sufficient number events with dimming and CME parameterizations to establish a significant correlation. Table 5.2 provides the Pearson correlation coefficients (Pearson, 1895) and p-value permutation statistical tests between each combination of the dimming and CME parameters, which confirms our initial expectation. Smaller p-values indicate a lower probability that the correlation could have arisen if no correlation existed at all. There is positive correlation between all of the parameter permutations, which is likely due to the "big flare syndrome" (Kahler, 1982, 1992), e.g., a rapid, powerful coronal magnetic field energy release tends to result in a faster, more massive CME.

Table 5.2: Pearson correlation coefficients (PCC) and p-values between dimming and CME parameters.

Parameter 1	Parameter 2	PCC	p-value
Slope	Speed	0.78	1.51×10^{-4}
Depth	Mass	0.74	7.80×10^{-4}
Slope	Mass	0.60	0.01
Depth	Speed	0.51	0.04
Mass	Speed	0.64	2.79×10^{-3}
Slope	Depth	0.27	0.15

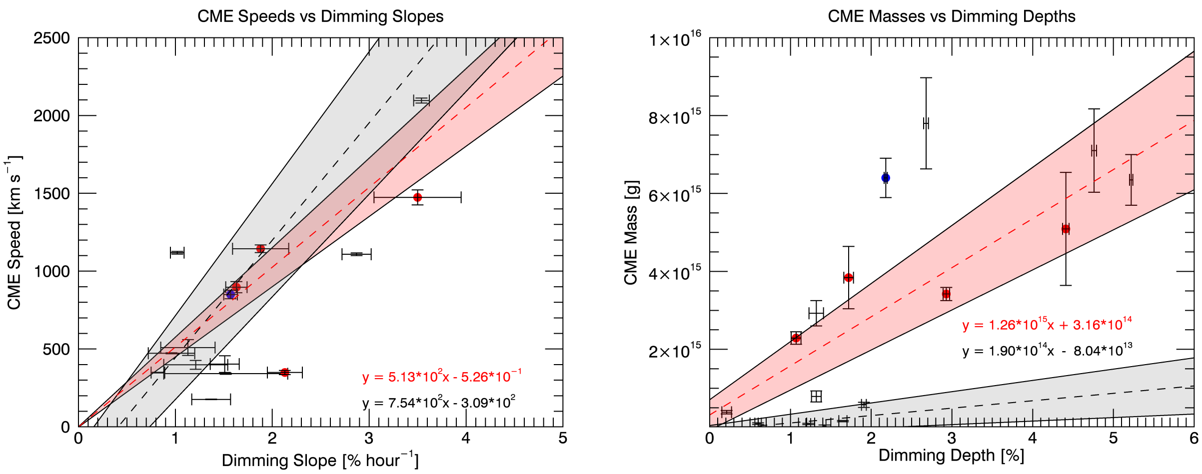

Figure 5.6: Scatterplots of (left) CME speed and dimming slope and (right) CME mass and dimming depth. Data without a center-point are derived from a single viewpoint of CMEs and are thus presented as a range of possible values rather than a single point with a standard uncertainty. Red symbols, line, and text indicate 3-D computed CME parameters, and the blue symbol indicates data from the simple 2010 August 7 event, which is also 3-D derived. Linear fits are shown as the dashed lines, and the grey/pink region represents the 3 uncertainty of the linear fits.

Figure 5.6 shows scatterplots of speed vs. slope and mass vs. depth with estimated error bars. Linear fits for each scatterplot were computed using IDL's *fitexy*, which can accept input errors in both axes and return the fit parameters with a 1σ uncertainty. The fit uncertainty is converted to 3σ and used to define the grey/pink regions of Figure 5.6. The fit equations are also listed in the Figure 5.6 panels. This process was repeated using only CME values computed from the 3-D methods and are plotted as the red dashed line and pink shaded region. In order to get a nominal fit for the 3-D case with so few data points, a virtual (0, 0) point was added to the fit.

The mass vs. depth plot (Figure 5.6, right) is linear-linear for clarity of the fits, but several of the data points end up off scale as they are $< 1 \times 10^{15}$ g. These points skew the fit uncertainty (grey area) significantly. Figure 5.7 is analogous to Figure 5.6, but shows the fit applied to high-mass only and low-mass only separately. The fit for high-mass only shows a slope that is less than a factor of two different from the all-points and 3-D points fits, whereas the fit for low-mass shows a slope that is an order of magnitude different from the others. When ignoring the low-mass points, the fit uncertainty narrows and is less skewed (grey area) and nearly all points fall within the uncertainty, when accounting for the uncertainty of the individual mass points. Thus, we suspect there may be two statistical families in the data. We examined all of these events individually and didnt notice any dimming or CME peculiarities that might cause this separation of high-mass and low-mass families in this comparison. The families do not strongly correlate to GOES flare magnitude (or whether there was a flare at all), CME span, or flare type. This result may be an artifact of small number statistics, which could be remedied in future work with many more dimming-CME events.

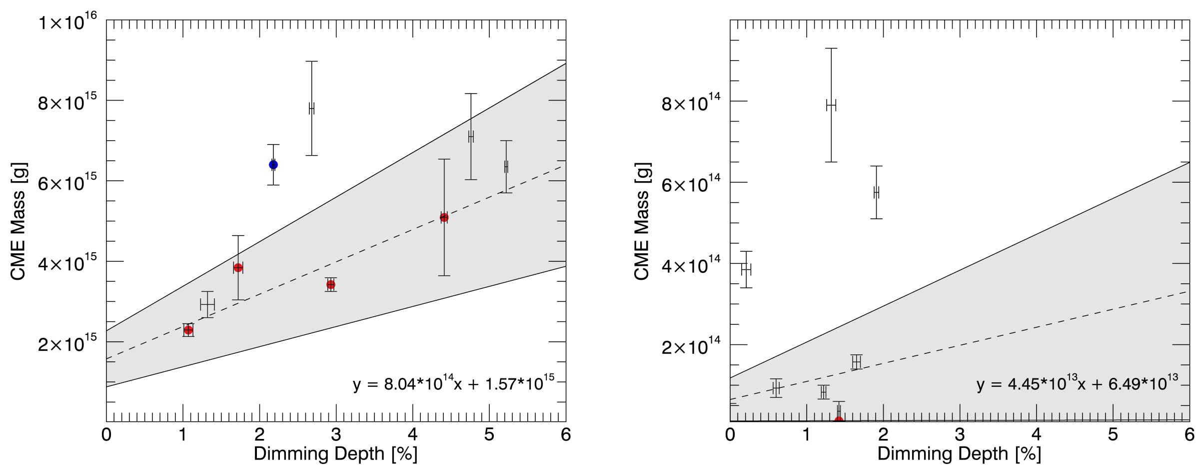

Figure 5.7: Same as Figure 5.6 but for (left) high CME mass ($\geq\ 1 \times 10^{15}\ g$) and dimming depth and (bottom) low CME mass ($< 1 \times 10^{15} g$) and dimming depth.

The 1σ uncertainties were computed by *fitexy* for each of these linear fits (note that the shaded regions in Figure 5.6 are 3σ). For all-points CME speed versus dimming slope, the fit slope is $7.54 \times 10^2 \pm 9.45 \times 10^1$ and fit y-intercept is $-3.09 \times 10^2 \pm 5.83 \times 10^1$. Assuming a y-intercept of zero and averaging the black and red slopes in Figure 5.6 left, the best estimate for the linear relationship is that the CME speed is 630 $km\ s^{-1}$ times the dimming slope (% $hour^{-1}$).

For CME mass vs dimming depth, the fit slope is $1.90 \times 10^{14} \pm 3.31 \times 10^{13}$ and fit y-intercept is $8.04 \times 10^{13} \pm 4.15 \times 10^{13}$. Averaging the 3D-derived and high-mass-only slopes, the best estimate for the linear relationship is that the CME mass is $1.03 \times 10^{15} g$ times the dimming depth (%).

Uncertainties are not factored into the Pearson correlation coefficients quoted in Table 5.2. Future work could use additional techniques for correlation that account for uncertainty, e.g., rank order. Such a study could include many more events to maximize the efficacy of the correlation comparison.

5.7 Summary

Positive correlations with a high degree of significance have been found between coronal dimming and CME parameters, providing evidence for our initial hypotheses that 1) dimming slope should be directly proportional to CME velocity, and 2) dimming depth should be directly proportional to CME mass. This existence of the correlation was predicted by physical theory. Linear fits between dimming slope and CME speed and between dimming depth and CME mass are provided in Section 5.6. Additionally, we found that the Fe IX 171 Å dimming corrected for the flare contributions using the Fe XV 284 Å line provides the most accurate dimming results for the EVE data. We note that the uncertainties for coronagraph and dimming parameters are complimentary: there are smaller uncertainties for CME speed than dimming slope, and there are smaller uncertainties for dimming depth than CME mass.

Bibliography

Andretta, V., Del Zanna, G., and Jordan, S. D. (2003). The EUV helium spectrum in the quiet Sun: A by-product of coronal emission? Astronomy and Astrophysics, 400(2):737–752.

Aschwanden, M. J. (2009). 4-D modeling of CME expansion and EUV dimming observed with STEREO/EUVI. Annales Geophysicae, 27(8):3275–3286.

Aschwanden, M. J., Nitta, N. V., Wuelser, J.-P., Lemen, J. R., Sandman, A., Vourlidas, A., and Colaninno, R. C. (2009a). First Measurements of the Mass of Coronal Mass Ejections From the EUV Dimming Observed With Stereo EUVI A + B Spacecraft. The Astrophysical Journal, 706(1):376–392.

Aschwanden, M. J., Wuelser, J. P., Nitta, N. V., and Lemen, J. R. (2009b). Solar Flare and CME Observations with STEREO/EUVI. Solar Physics, 256(1-2):3–40.

Attrill, G. D. R., Harra, L. K., van Driel-Gesztelyi, L., and Wills-Davey, M. J. (2010). Revealing the Fine Structure of Coronal Dimmings andAssociated Flows withHinode/EIS. Solar Physics, 264(1):119–147.

Bein, B. M., Temmer, M., Vourlidas, A., Veronig, A. M., and Utz, D. (2013). THE HEIGHT EVOLUTION OF THE TRUE CORONAL MASS EJECTION MASS DERIVED FROM STEREO COR1 AND COR2 OBSERVATIONS. 31.

Bevington, P. (2003). Data reduction and error analysis for the physical sciences. McGraw-Hill, Boston.

Bewsher, D., Harrison, R. A., and Brown, D. S. (2008). The relationship between EUV dimming and coronal mass ejections I. Statistical study and probability model. Astronomy & Astrophysics, 478:897–906.

Caspi, A., McTiernan, J. M., and Warren, H. P. (2014). CONSTRAINING SOLAR FLARE DIFFERENTIAL EMISSION MEASURES WITH EVE AND RHESSI. The Astrophysical Journal, 788(2):L31.

Chen, P. F., Fang, C., and Shibata, K. (2005). A Full View of EIT Waves. The Astrophysical Journal, 622(2):1202–1210.

Chen, P. F., Wu, S. T., Shibata, K., and Fang, C. (2002). Evidence of EIT and Moreton Waves in Numerical Simulations. The Astrophysical Journal, 572(1):L99–L102.

Colaninno, R. C. and Vourlidas, A. (2009). First Determination of the True Mass of Coronal Mass Ejections: A Novel Approach To Using the Two Stereo Viewpoints. The Astrophysical Journal, 698:852–858.

Colaninno, R. C., Vourlidas, A., and Wu, C. C. (2013). Quantitative comparison of methods for predicting the arrival ofcoronal mass ejections at Earth based on multiview imaging. Journal of Geophysical Research: Space Physics, 118(11):6866–6879.

Fletcher, L., Dennis, B. R., Hudson, H. S., Krucker, S., Phillips, K., Veronig, A. M., Battaglia, M., Bone, L., Caspi, A., Chen, Q., Gallagher, P. T., Grigis, P. T., Ji, H., Liu, W., Milligan, R. O., and Temmer, M. (2011). An Observational Overview of Solar Flares. Space Science Reviews, 159(1-4):19–106.

Gilbert, H. R., Inglis, a. R., Mays, M. L., Ofman, L., Thompson, B. J., and Young, C. a. (2013). Energy Release From Impacting Prominence Material Following the 2011 June 7 Eruption. The Astrophysical Journal, 776(1):L12.

Giordano, S., Antonucci, E., and Dodero, M. (2000). OXYGEN VELOCITIES IN A POLAR CORONAL. Advances in Space Research, 25(9):1927–1930.

Gopalswamy, N., Yashiro, S., Michalek, G., Stenborg, G., Vourlidas, A., L, F. S., and Howard, R. A. (2009). The SOHO / LASCO CME Catalog. Earth Moon Planet, 104:295–313.

Greenstein, J. L. (1958). High-Resolution Spectra of Comet MRKOS. The Astrophysical Journal, 128:106.

Harra, L. K., Mandrini, C. H., Dasso, S., Gulisano, A. M., Steed, K., and Imada, S. (2010). Determining the Solar Source of a Magnetic Cloud Using a Velocity Difference Technique. Solar Physics, 268(1):213–230.

Harra, L. K. and Sterling, A. C. (2001). Material Outflows from Coronal Intensity "Dimming Regions" During Coronal Mass Ejection Onset. The Astrophysical Journal Letters, 561:215–218.

Harrison, R. A., Bryans, P., Simnett, G. M., and Lyons, M. (2003). Coronal dimming and the coronal mass ejection onset. Astronomy & Astrophysics, 400:1071–1083.

Harrison, R. A. and Lyons, M. (2000). A spectroscopic study of coronal dimming associated with a coronal mass ejection. Astronomy & Astrophysics, 1108:1097–1108.

Hudson, H. S., Acton, L. W., and Freeland, S. L. (1996). A Long-Duration Solar Flare with Mass Ejection and Global Consequences. The Astrophysical Journal, 470:629–635.

Hudson, H. S., Lemen, J. R., St. Cyr, O. C., Sterling, A. C., and Webb, D. F. (1998). X-ray coronal changes during halo CMEs. Geophysical Research Letters, 25(14):2481–2484.

Hudson, H. S., Woods, T. N., Chamberlin, P. C., Fletcher, L., Zanna, G. D., Didkovsky, L., Labrosse, N., and Graham, D. (2011). The EVE Doppler Sensitivity and Flare Observations. Solar Physics, 273:69–80.

Hyder, C. L. and Lites, B. W. (1970). H-alpha Doppler Brightening and Lyman-alpha Doppler Dimming in Moving H-alpha Prominences. Solar Physics, 14(1):147–156.

Imada, S., Hara, H., Watanabe, T., Kamio, S., Asai, A., Matsuzaki, K., Harra, L. K., and Mariska, J. T. (2007). Discovery of a Temperature-Dependent Upflow in the Plage Region during a Gradual Phase of the X-Class Flare. Publications of the Astronomical Society of Japan, 59(sp3):S793–S799.

Jin, M., Ding, M. D., Chen, P. F., Fang, C., and Imada, S. (2009). CORONAL MASS EJECTION INDUCED OUTFLOWS OBSERVED WITH HINODE /EIS. The Astrophysical Journal, 702(1):27–38.

Kahler, S. (1992). Solar Flares and Coronal Mass Ejections. Annual Review of Astronomy and Astrophysics, 30:113–141.

Kahler, S. W. (1982). The role of the big flare syndrome in correlations of solar energetic proton fluxes and associated microwave burst parameters. Journal of Geophysical Research, 87(A5):3439.

Krista, L. D. and Reinard, A. (2013). STUDY OF THE RECURRING DIMMING REGION DETECTED AT AR 11305 USING THE CORONAL DIMMING TRACKER (CoDiT). The Astrophysical Journal, 762(2):91.

Labrosse, N. and Mcglinchey, K. (2012). Plasma diagnostic in eruptive prominences from SDO / AIA observations at 304 Å. Astronomy & Astrophysics, 537:A100.

Liu, W. and Ofman, L. (2014). Advances in Observing Various Coronal EUV Waves in the SDO Era and Their Seismological Applications (Invited Review). Solar Physics, 289(9):3233–3277.

Mason, J. P., Woods, T. N., Caspi, A., Thompson, B. J., and Hock, R. A. (2014). MECHANISMS AND OBSERVATIONS OF CORONAL DIMMING FOR THE 2010 AUGUST 7 EVENT. The Astrophysical Journal, 789(1):61.

Muhr, N., Veronig, A. M., Kienreich, I. W., and Temmer, M. (2011). Analysis of Characteristic Parameters of Large-Scale Coronal Waves Observed by the Solar-Terrestrial Relations Observatory/Extreme Ultraviolet Imager. The Astrophysical Journal, 89:89.

Pearson, K. (1895). Note on Regression and Inheritance in the Case of Two Parents. Proceedings of the Royal Society of London, 58:240–242.

Pohjolainen, S., Vilmer, N., Khan, J. I., and Hillaris, A. E. (2005). Early signatures of large-scale field line opening Multi-wavelength analysis of features connected with a halo CME event. Astronomy & Astrophysics, 434:329–341.

Reinard, A. A. and Biesecker, D. A. (2008). Coronal Mass Ejection-Associated Coronal Dimmings. The Astrophysical Journal, 674:576–585.

Reinard, A. A. and Biesecker, D. A. (2009). The Relationship Between Coronal Dimming and Coronal Mass Ejection Properties. The Astrophysical Journal, 705(1):914–919.

Robbrecht, E. and Wang, Y.-M. (2010). The Temperature-Dependent Nature of Coronal Dimmings. The Astrophysical Journal Letters, 720:88–92.

Rompolt, . (1967). The Hα Radiation Field in the Solar Corona for Moving Prominences. Acta Astronomica, 17.

Schrijver, C. J. and Higgins, P. A. (2015). A Statistical Study of Distant Consequences of Large Solar Energetic Events. Solar Physics, 290(10):2943–2950.

Sterling, A. C. and Hudson, H. S. (1997). YOHKOH SXT OBSERVATIONS OF X-RAY DIMMING ASSOCIATED WITH A HALO CORONAL MASS EJECTION. The Astrophysical Journal, 491:L55–L58.

Swings, P. (1941). Complex Structure of Cometary bands Tentatively Ascribed to the Contour of the Solar Spectrum. Lick Observatory Bulletin, 508.

Thompson, B. J., Cliver, E. W., Nitta, N. V., Delannée, C., and Delaboudiniere, J. P. (2000). Coronal Dimmings and Energetic CMEs in April-May 1998. Geophysical Research Letters, 27(10):1431–1434.

Tian, H., McIntosh, S. W., Xia, L., He, J., and Wang, X. (2012). What Can We Learn About Solar Coronal Mass Ejections, Coronal Dimmings, and Extreme-Ultraviolet Jets Through Spectroscopic Observations? The Astrophysical Journal, 748(2):106.

Vourlidas, a., Howard, R. a., Esfandiari, E., Patsourakos, S., Yashiro, S., and Michalek, G. (2010). Comprehensive Analysis of Coronal Mass Ejection Mass and Energy Properties Over a Full Solar Cycle. The Astrophysical Journal, 722(2):1522–1538.

Woods, T. N., Hock, R. A., Eparvier, F. G., Jones, A. R., Chamberlin, P. C., Klimchuk, J. A., Didkovsky, L., Judge, D., Mariska, J. T., Warren, H. P., Schrijver, C. J., Webb, D. F., Bailey, S. M., and Tobiska, W. K. (2011). New Solar Extreme-Ultraviolet irradiance Observations During Flares. The Astrophysical Journal, 739:59.

Zhukov, A. N. and Auchère, F. (2004). On the nature of EIT waves, EUV dimmings and their link to CMEs. Astronomy & Astrophysics, 427:705–716.

Appendix A

Coronal Dimming Event List and Ancillary Data